Quarterly Report for

Contract DE-FG36-08GO18192

Stanford Geothermal Program

April-June 2009

Table of Contents

1. FRACTURE CHARACTERIZATION USING PRODUCTION AND INJECTION DATA

This research project is being conducted by Research Assistant Egill Juliusson, Senior Research Engineer Kewen Li and Professor Roland Horne. The objective of this project is to investigate ways to characterize fractures in geothermal reservoirs using injection and production data.

1.1 SUMMARY

This project involves fracture characterization, utilizing advanced mathematical analysis to extract information from production data.

This report introduces a statistics-based deconvolution method which has been used to extract core information from production data. As a test, the production data were generated from multiple input signals, and the deconvolution method was designed to reveal the transfer function from each input to the output. The transfer functions that were obtained are equivalent to tracer return curves, and can therefore be used to answer multiple questions relating to reservoir management. This method also opens up the possibility of injecting the same type of tracer into multiple wells at similar times and analyzing the results for individual well-to-well fracture connections under actual production conditions. The results so far have been produced using random synthetic data sets generated from analytical formulations.

Currently effort is being put into posing the deconvolution problem in such a manner that it will yield a unique solution over the entire time domain. It appears that the key to creating a feasible objective function will depend on the injection pattern of the tracer and the formulation of the roughness penalty term used to constrain the desired solution. Added physical constraints might also prove useful, e.g. mass conservation and nonnegativity constraints.

1.2 IMPORTANCE OF UNDERSTANDING WELL-TO-WELL INTERACTION

Understanding well-to-well interaction is of much importance in geothermal reservoir engineering. Tracer tests are commonly performed to gain such an understanding and various estimates can be made from the return curves. For example, the total reservoir volume and the efficiency of heat recovery can be estimated, which very important for reducing uncertainty in volumetric Monte Carlo models. These are commonly used e.g. by the USGS for the National Geothermal Resource Estimate, and in the early stages of geothermal project development. At later stages, tracer return curves can be used to predict the expected decline in production temperature with time, and the allowable increase in energy production from underutilized reservoirs, as shown by Axelsson et al. (2001).

In a more advanced application, Lovekin (1989) illustrated the usefulness of well-to-well interaction data for optimizing reinjection scheduling. The essence of the approach was to minimize the field-wide risk of thermal breakthrough. This required an estimate of a connectivity parameter quantifying the risk of breakthrough between each injector-producer pair in the field. Multiple parameters were suggested for quantifying the

connectivity, many of which would be obtained from tracer tests (e.g. initial and peak return time, peak return concentration and cumulative tracer return), but the vertical and horizontal distance between the wells in question were also recommended. Given the connectivity parameter, the scheduling problem could be set up as a constrained quadratic program which was solved to find the optimal injection and production rates.

A considerable drawback to Lovekin's approach was associated with obtaining the connectivity data. This could be obtained by performing tracer tests for each injection well. That is however a nontrivial task and requires either the use of different types of tracer for each injection well, or waiting a long time (years) between tests on each individual injection well. Finding way to determine the origins of a tracer signal based solely on the transients of the input and output is one of the goals of this work, thus allowing the application of tracer tests on multiple wells simultaneously with only one type of tracer.

1.3 DECONVOLUTION MODELING

Deconvolution can be seen as an extension of the regression techniques discussed in the last quarterly report for this project (Winter 2009). The advantage of using a convolution model is that it inherently takes account of the time-lag between injection and production and it provides more that just the travel time between wells (e.g. dispersivity and fraction of tracer returned). The main disadvantage is that more densely collected data samples are needed to obtain meaningful results.

A statistically-derived approach is suggested here, which fits well with our emphasis on using models that allow a suitable level of information extraction while imposing only minimal constraints on the underlying relationship between the injection and production data. At this point the study has focused on the analysis of tracer return data, although information extraction from other data types such as pressure, temperature or enthalpy is conceivable.

1.3.1 Multiwell deconvolution based on Bayesian statistics

The method applied here is based on the assumption that well-to-well connectivity can be characterized by the convolution Equation (1.1). This implies that the production, $c_p(t)$, at one well can be described as a weighted sum of previous injection, $c_r(t)$, into another well. The weights, $\kappa(t)$, depend on the time lag between injection and production and form a curve referred to as the kernel. The integral of this curve over time is analogous to a tracer return curve from a slug injection tracer test (within a multiplicative constant, depending on the mass injected).

$$c_p(t) = \int_0^t c_r(t-\tau)\kappa(\tau)d\tau \tag{1.1}$$

Equation (1.1) can be represented in discretized form as:

$$\vec{c}_p = H\vec{\kappa} + \vec{v} \tag{1.2}$$

where H is an n by m matrix, n is the number of conditioning data points and m is the number of discretization points for $\vec{\kappa}$. The vector $\vec{v}$ is a zero-mean vector representing measurement error with covariance matrix R, which is described in Equation (1.12). The kernel, $\vec{\kappa}$, is the unknown to be estimated.

Methods for solving equations like (1.2) numerically, with weak prior assumptions based on Bayesian statistics have been discussed for example by Finen et al. (2006) and Kitanidis (2009). These assumptions are weak in the sense that they only set limits to the variability of the outcome, $\vec{\kappa}$, and the extent to which the conditioning data, $\vec{c}_p$, needs to be reproduced.

Using the approach of Kitanidis (2009), one defines a prior model for the kernel,

$$\kappa(t) = \sum_{k=1}^{p} f_k(t)\beta_k + \varepsilon(t) \tag{1.3}$$

where f_k is a known function (e.g. a constant or a line), β_k, are unknown coefficients and $\varepsilon(t)$ represents stochastic noise with zero mean and a given covariance function. The expected mean and covariance of Equation (1.3) are represented as:

$$E[\vec{\kappa}] = X\vec{\beta} \tag{1.4}$$

and

$$E\left[(\vec{\kappa} - \mu)(\vec{\kappa} - \mu)^T\right] = Q \tag{1.5}$$

Now through Bayesian analysis, assuming that the prior probability density function (pdf) is Gaussian, it can be shown that the maximum posterior likelihood estimate of $\vec{\kappa}$ is:

$$\vec{\kappa} = \Lambda\vec{c}_p \tag{1.6}$$

where Λ is found by solving the linear system:

$$\begin{bmatrix} HQH^T + R & HX \\ (HX)^T & 0 \end{bmatrix}\begin{bmatrix} \Lambda^T \\ M \end{bmatrix} = \begin{bmatrix} HQ \\ X^T \end{bmatrix} \tag{1.7}$$

Continued analysis allows the computation of the posterior covariance, V, and there by the confidence intervals for $\vec{\kappa}$:

$$V = -XM + Q - QH^T\Lambda \tag{1.8}$$

Methods for generating conditional realizations are also easily applicable, and these have been implemented, although the relevant formulations will not be recited here.

The elements of the H matrix representing the injection will have the formulation described by Equation (1.9), assuming a Riemann numerical integration scheme with discretization $\tau_j = \Delta\tau/2 + (j-1)\Delta\tau$ where $j \in \{1,..., m\}$:

$$H_{ij} = \begin{cases} c_r(t_i - \tau_j)\Delta\tau, & t_i > \tau_j - \dfrac{\Delta\tau}{2} \\ 0 & t_i <= \tau_j - \dfrac{\Delta\tau}{2} \end{cases} \tag{1.9}$$

The structural matrices, X, Q, and R, used to formulate the aforementioned inversion are of importance. The prior trend matrix X is commonly chosen with $X_{j1} = 1$ for a constant mean and a linear trend can be added by adding a second column $X_{j2} = \tau_j$, $j \in \{1,..., m\}$. The generalized covariance matrix of the prior, Q, can be formulated, e.g. using:

$$Q_{ij} = -\theta_Q\left|\tau_i - \tau_j\right| \tag{1.10}$$

which corresponds to a constant mean assumption. Or if a linear trend is added, an appropriate covariance matrix is:

$$Q_{ij} = \theta_Q \left| \tau_i - \tau_j \right|^3 \tag{1.11}$$

Finally the covariance matrix for the measurement error is formulated as:

$$R = \theta_R I \tag{1.12}$$

where I is the n by n identity matrix. The structural parameters, θ_Q and θ_R, that in a sense provide the optimum balance between reproducing the data and suppressing noise, can be found. The procedure is related to cross-validation and basically involves linearly transforming the data into a space where it has zero mean and then constraining the normalized residuals to have unit variance (see Kitanidis, 1997).

The deconvolution method described so far has been generalized to handle the case where there are multiple (N_r) injectors, i.e. where the response in the producer is described by:

$$c_p(t) = \sum_{k=1}^{N_r} \int_0^t c_{rk}(t-\tau)\kappa_k(\tau) d\tau \tag{1.13}$$

In this case the discrete form becomes:

$$\vec{c}_p = \sum_{k=1}^{N_r} H_k \vec{\kappa}_k + \vec{v} = H\vec{\kappa} + \vec{v} \tag{1.14}$$

where now:

$$H = \left[H_1 \; H_2 \ldots H_{N_r} \right] \tag{1.15}$$

And:

$$\kappa = \left[\kappa_1 \; \kappa_2 \ldots \kappa_{N_r} \right]^T \tag{1.16}$$

In this case the matrix X is also extended to a matrix with $N_r \times m$ rows. Finally, the the generalized covariance matrix, Q becomes a block-diagonal matrix with $m \times m$ diagonal blocks, Q_k, defined as in Equation (1.10) or (1.11), with separate multipliers, θ_{Q_k}, for each block.

1.3.2 Application of multiwell deconvolution approach

A preliminary investigation of the applicability of the multiwell deconvolution approach has been performed. Synthetic production data was generated for a case with two injectors and one producer. The data were generated using an analytical solution of the one dimensional advection-dispersion equation, specifically the finite-impulse response on an infinite domain, i.e.:

$$c_p(t) = \frac{m}{\sqrt{4\pi D t}} \exp\left[-\frac{(x-ut)^2}{4Dt} \right] \tag{1.17}$$

where c_p is the produced concentration [kg/m], m is the injected mass [kg], D is the dispersivity coefficient [m^2/s], x is the distance between the wells [m], and u is the mean flow velocity [m/s]. The relationship between mass and concentration can be written as:

$$m = c_r(t) u dt \tag{1.18}$$

where c_r is the concentration of injected fluid and dt is the duration of the injection pulse. This can be substituted into (1.17) to obtain any given response through convolution (i.e. superposition):

$$c_p(t) = \int_0^t \frac{c_r(t-\tau)u}{\sqrt{4\pi D\tau}} \exp\left[-\frac{(x-u\tau)^2}{4D\tau}\right] d\tau \tag{1.19}$$

So in this case the kernel has the formulation:

$$\kappa(t) = \frac{u}{\sqrt{4\pi Dt}} \exp\left[-\frac{(x-ut)^2}{4Dt}\right] \tag{1.20}$$

Note that the kernel depends only on the characteristics of the well-to-well connection, and not the mass or concentration of tracer injected. The kernel is however dependent on the amount of injected fluid, through the average flow velocity, *u*. This means that meaningful kernel estimations require that the fluid injection and production rates stay constant (or close to constant), but the amount of injected tracer can and should vary.

A few simple examples were designed to illustrate the extents to which the method is applicable.

1.3.2.1 Example 1: Effects of varying injection history

In the first example, the effects of varying injection history were investigated. Two synthetic kernels were created, using Equation (1.20), as shown in Figure 1.1.

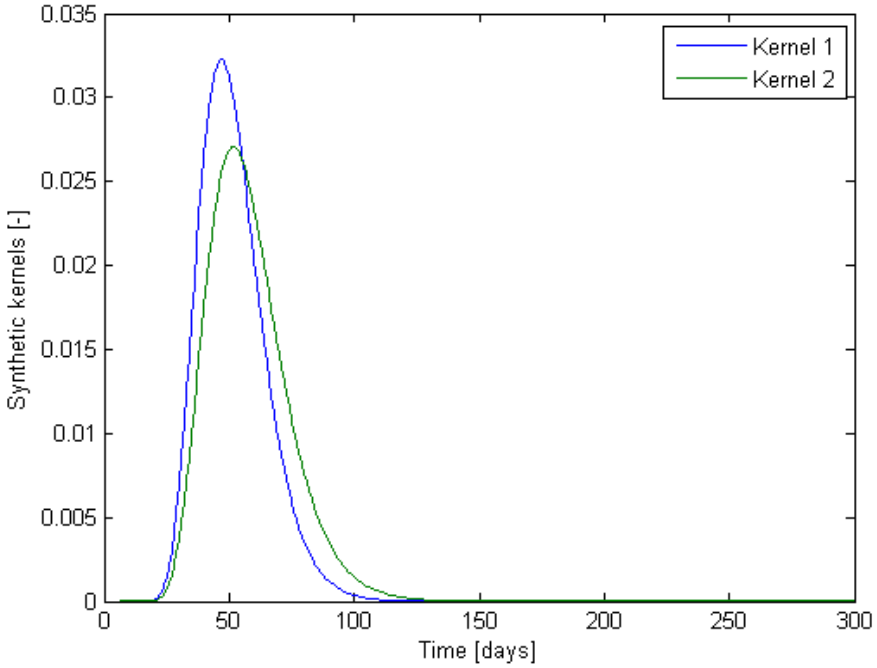

Figure 1.1: Synthetic kernels created for Example 1. Kernel 1 has, x=221m, D=33.7m^2/day, and u=4.58m/day. Kernel 2 has, x=153m, D=16.8 m^2/day, and u=2.86m/day.

A random injection history was created, and the corresponding production history was calculated using Equation (1.19). The injection and production data are shown in Figure 1.2.

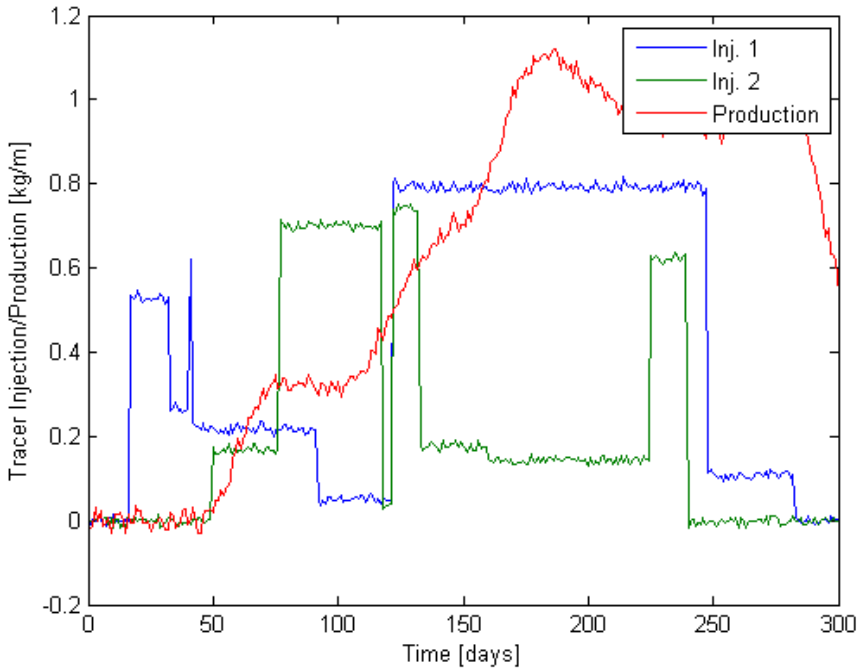

Figure 1.2: Random injection histories and the corresponding production history created from an analytical formulation. This is referred to as injection Case 1.

The multiwell deconvolution method was applied to the data from Case 1. The linear version of the covariance matrix, Q, was used and correspondingly the prior trend was assumed to be constant, i.e. X was a vector of ones. The order of magnitude of the structural parameters, θ's, was decided based on experimentation, but otherwise left untuned. The results in this case proved relatively accurate (given the limited assumptions about the outcome), as seen in Figures 1.3 and 1.4.

A noticeable increase in uncertainty is seen at late times, especially for kernel 2. This is understandable since the first change in injection for injector 2 occurs around day 50, and therefore there is no real data to constrain the last 50 days of the estimate for kernel 2.

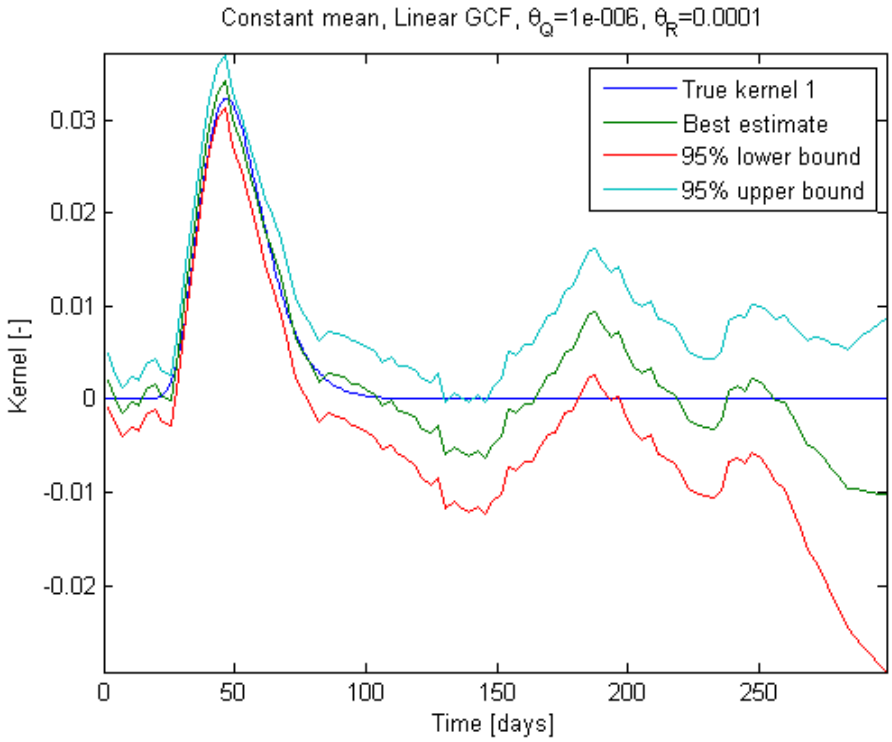

Figure 1.3: Best estimate and confidence intervals obtained for kernel 1, injection Case 1.

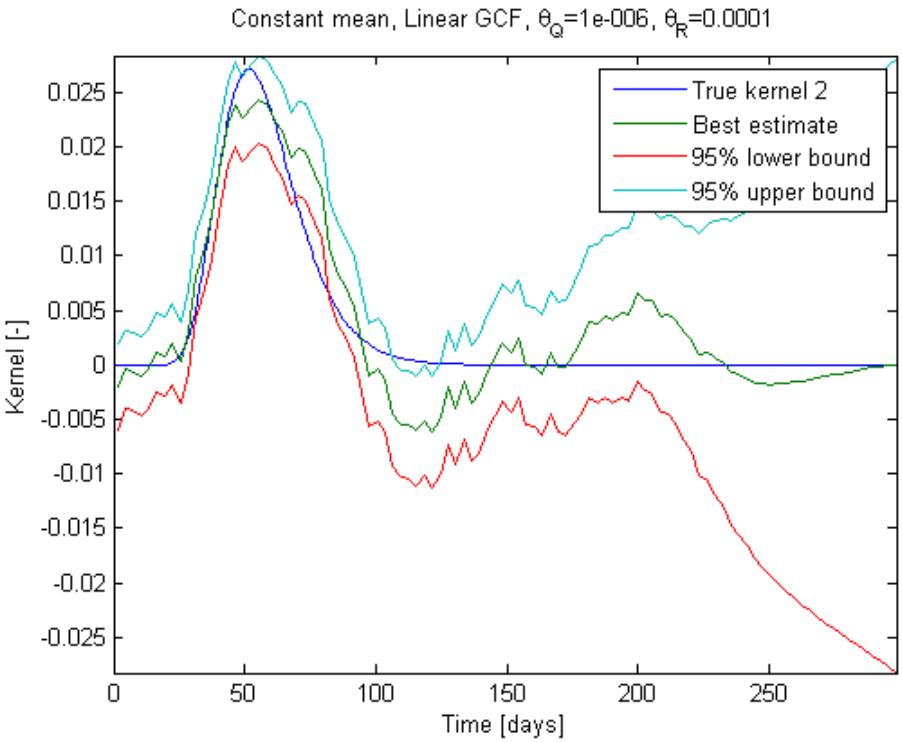

Figure 1.4: Best estimate and confidence intervals obtained for kernel 2, injection Case 1.

The reproduction of the measured data using these kernels was quite successful as shown in Figure 1.5.

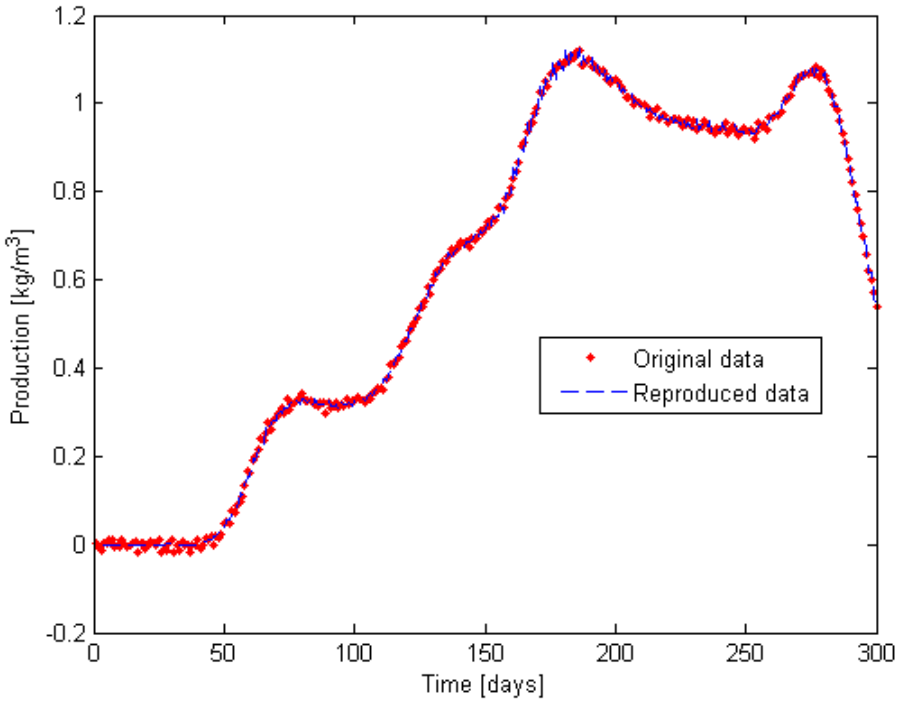

Figure 1.5:Reproduction of data using best estimates for kernels shown in Figures 1.4 and 1.5, injection Case 1.

Unfortunately, the relatively good results seen in Figures 1.3 and 1.4 are not representative for all injection histories. Take for example the injection histories shown in Figure 1.6. These do not seem so dramatically different from those shown in Figure 1.2, however, the best estimates for both kernels are quite far off, as seen in Figures 1.7 and 1.8.

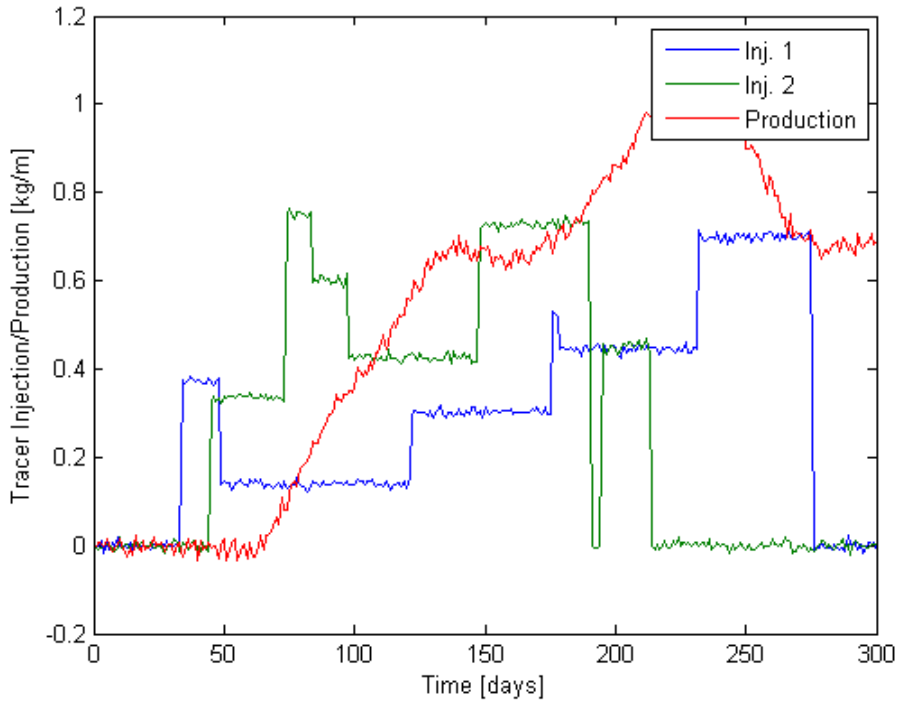

Figure 1.6: Random injection histories and the corresponding production history created from an analytical formulation. This is referred to as injection Case 2.

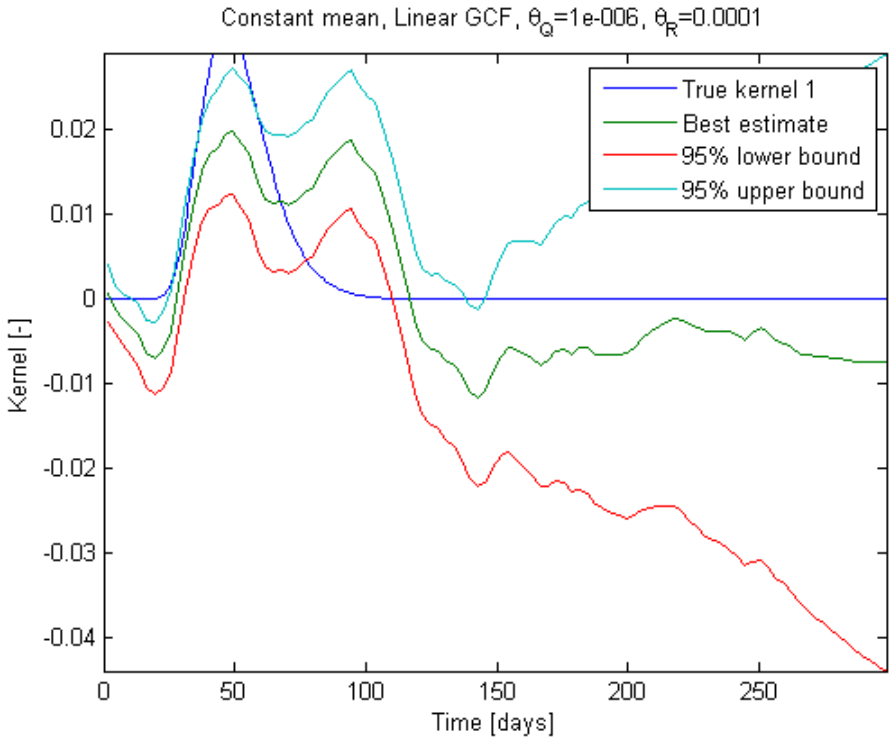

Figure 1.7: Best estimate and confidence intervals obtained for kernel 1, injection Case 2. This is an example of poor results.

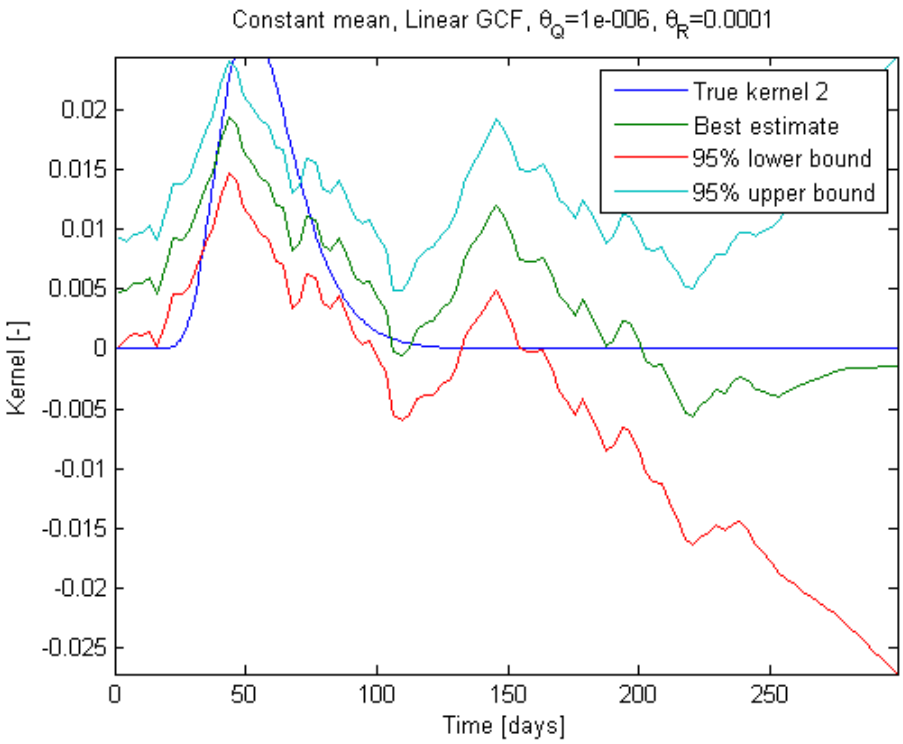

Figure 1.8: Best estimate and confidence intervals obtained for kernel 2, injection Case 2. This is an example of poor results.

In spite of the relatively poor reproduction of the given kernels, the production data was very successfully reproduced in this case, and the plot of the reproduced data in this case was almost identical to that shown in Figure 1.5.

It is philosophically understandable that certain uniqueness must exist in the ensemble of injection signals, for meaningful extraction of the underlying transfer function (kernel). The mathematical expression of this uniqueness remains a topic of future research.

1.3.2.2 Example 2: Dissimilar kernels and parameter tuning

Working with different kernels requires retuning of the structural parameters, θ, which control the balance between reproduction of the data, and smoothness in the solution. This can be done either manually or automatically. The automatic tuning is performed using a method called Restricted Maximum Likelihood, which basically transforms the production data into a space where it has zero mean and then constrains the normalized residuals to have a unit variance. The method is not infallible but works in most cases, and when it fails, it can often be mended by using a different initial guess for the θ values.

A case with more dissimilar kernels than in Example 1 is presented here, i.e. this means that one well is well connected to the producer (e.g. through a fracture), while the other has a more dispersive connection. A plot of the kernels is shown in Figure 1.9.

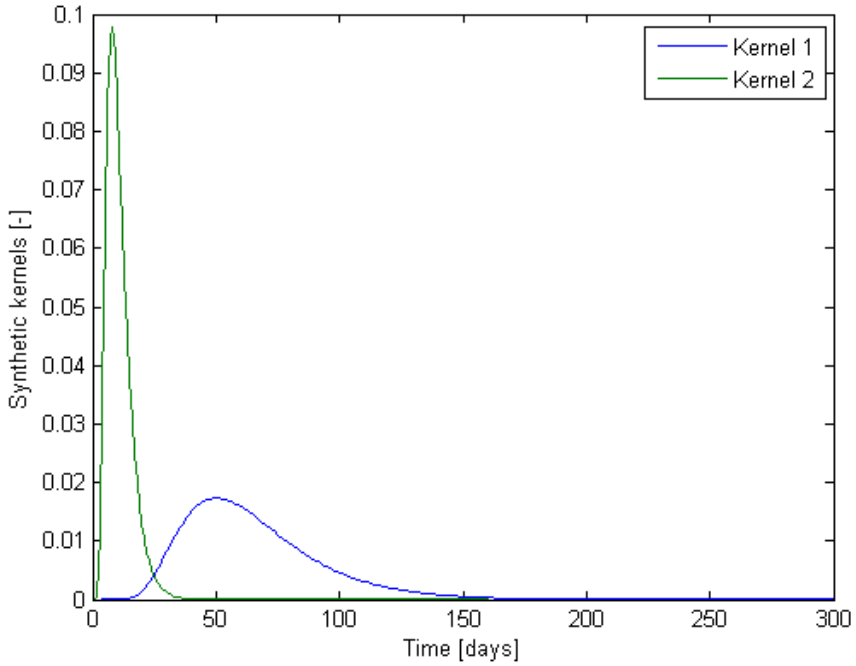

Figure 1.9: Synthetic kernels created for Example 2. Kernel 1 has, x=174m, D=50.7m^2/day, and u=3.16m/day. Kernel 2 has, x=172m, D=393m^2/day, and u=19.8m/day.

Case 1 was used for the injection histories but, the production history is different from the one shown in Figure 1.2 because the kernels are different. This is illustrated in Figure 1.10.

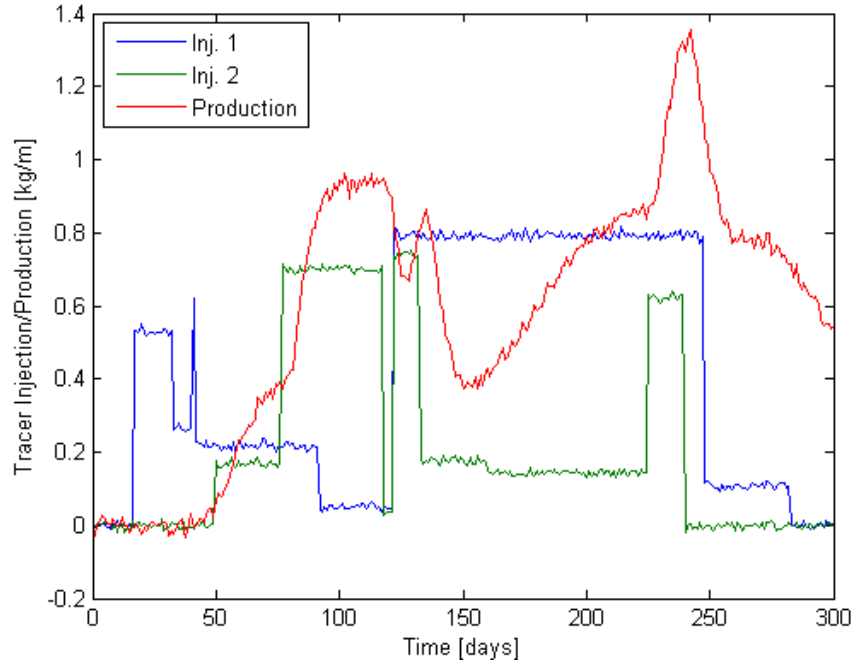

Figure 1.10: The injection history is the same as in Figure 1.2 but the production is different because different kernels are used in this example.

The deconvolution method was applied to the data shown in Figure 1.10, using automatic parameter tuning. The automatic tuning yielded a higher θ_Q value for kernel 2 since that tends to allow more variability in the solution, thereby allowing the reproduction of the relatively sharp peak. The estimates obtained are shown in Figures 1.11 and 1.12.

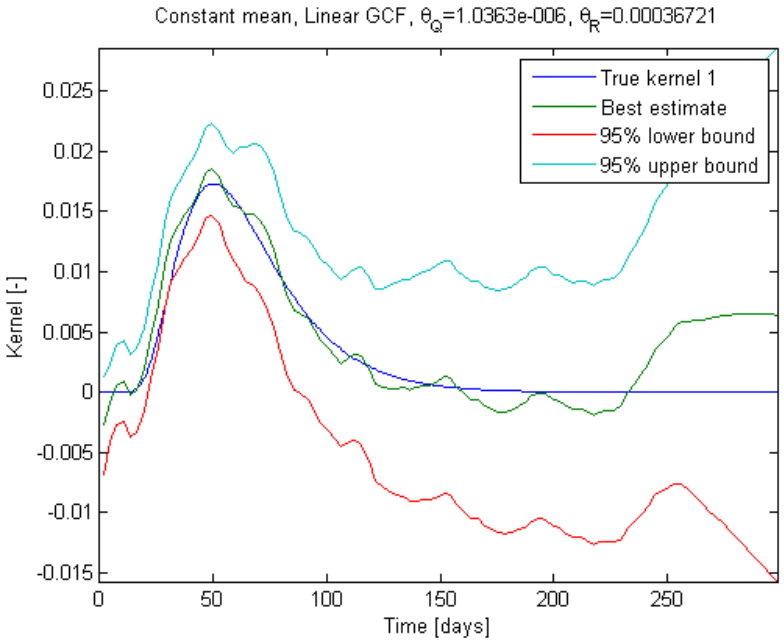

Figure 1.11: Best estimate and confidence intervals obtained for kernel 1, injection Case 1. A linear covariance matrix, Q, was used with a constant mean assumption for X.

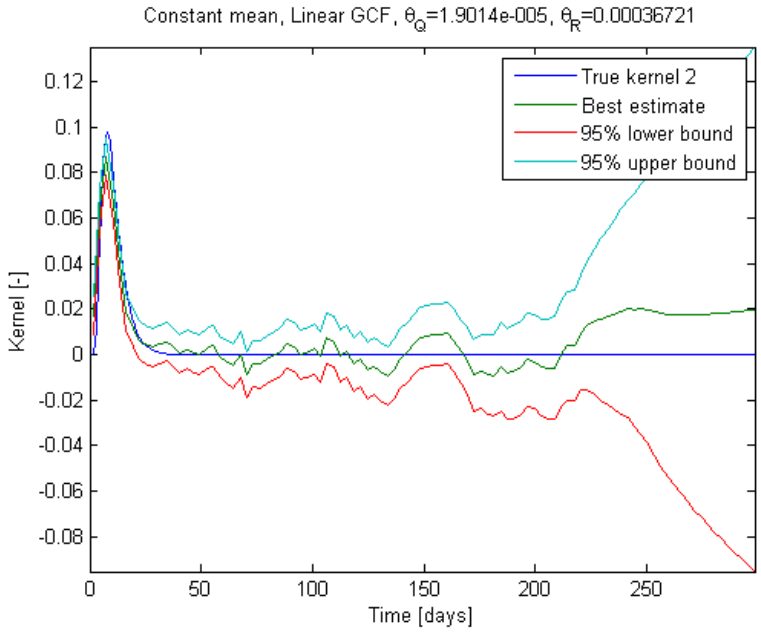

Figure 1.12: Best estimate and confidence intervals obtained for kernel 2, injection Case 1. A linear covariance matrix, Q, was used with a constant mean assumption for X.

This example shows that the multiwell deconvolution method has the ability to handle kernels of varying character, and the automatic tuning of structural parameters can be a useful tool for quickly finding the approximate shape of the kernel.

Slightly smoother solutions can be found using the cubic version of the roughness penalty covariance matrix, *Q*, as formulated in Equation (1.11). Such solutions are shown in Figures 1.13 and 1.14. A drawback to using the cubic covariance is that the large scale fluctuation in the solution tends to get larger, especially at late times, where there is less data to constrain the solution.

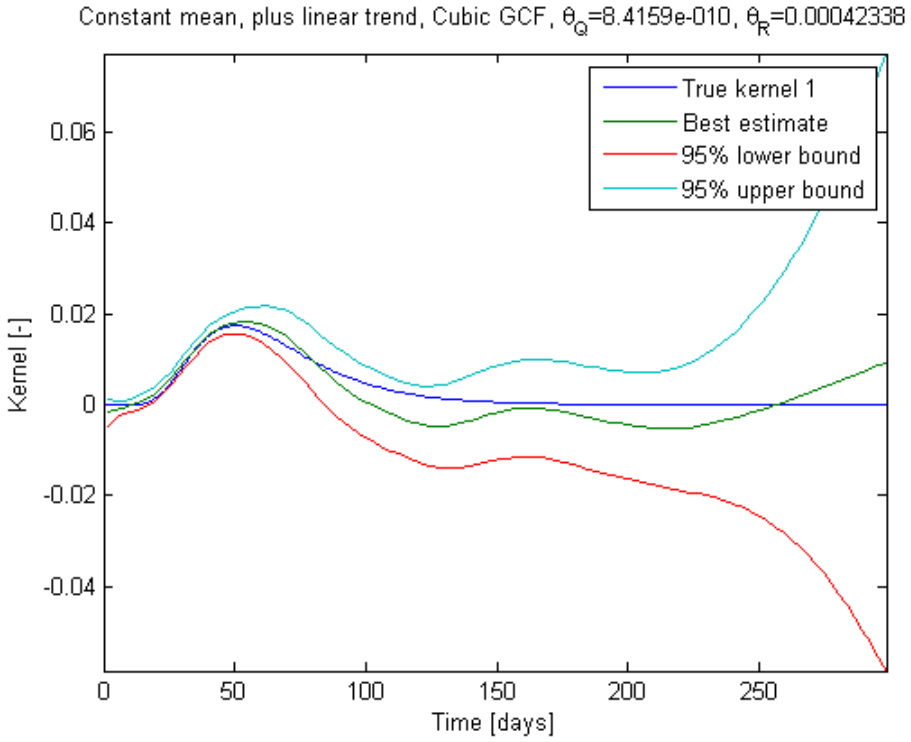

Figure 1.13: Best estimate and confidence intervals obtained for kernel 2, injection Case 1. A cubic covariance matrix, Q, was used with a linear trend assumption for X.

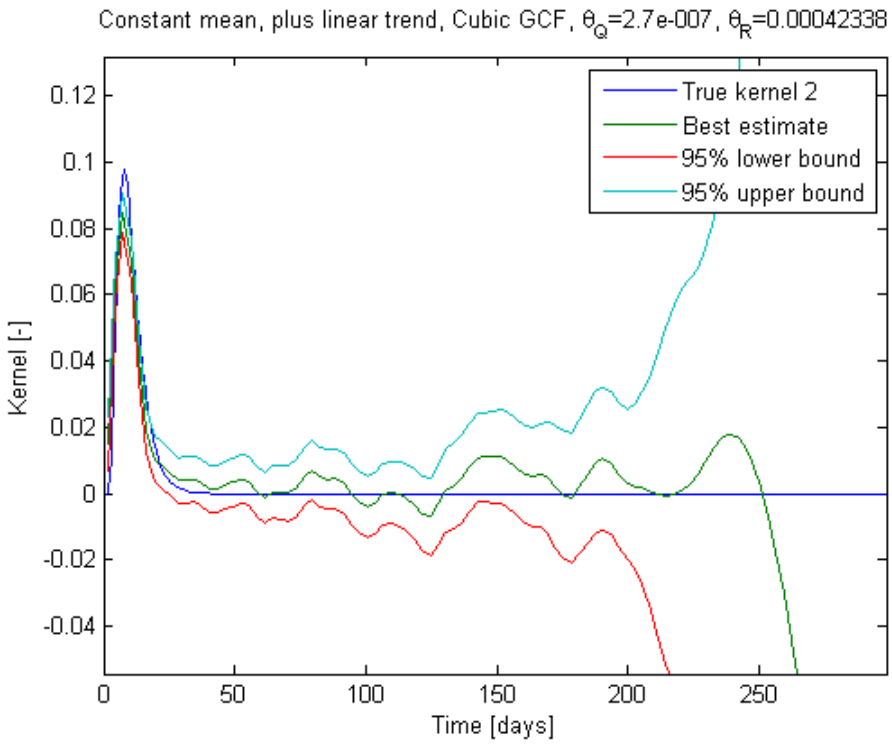

Figure 1.14: Best estimate and confidence intervals obtained for kernel 2, injection Case 1. A cubic covariance matrix, Q, was used with a linear trend assumption for X.

1.3.2.3 Example 3: Nonnegativity constraints

Some additional constraints can be added to the kernel estimation problem without assuming too much about the shape of the solution. One basic example is that the kernel can not be negative, i.e. the produced concentration will not get smaller because of an increase in injected concentration. Another example is given by Equation (1.21), which simply states that no more than the total mass injected into each well will come out in the production well.

$$\int_0^{t_{\max}} \kappa_k(t)dt \le 1, \quad k \in \{1,...,N_r\} \tag{1.21}$$

This example focuses on the former constraint, nonnegativity. A fairly simple way to enforce nonnegativity in the solution, is to rewrite the kernel in terms of a dummy variable, $\kappa = \exp(s)$, and therefore the deconvolution problem changes to:

$$c_p(t) = \int_0^t c_r(t-\tau)\exp(s(\tau))d\tau = h(s) \tag{1.22}$$

Now the kernel can clearly not become negative, but the deconvolution problem needs to be solved for the dummy variable, s, and is therefore nonlinear. However, starting with a good guess for, *s*, better estimates can be found iteratively by solving the system,

$$\vec{c}_p - h(\vec{s}_k) + \tilde{H}\vec{s}_k = \tilde{H}\vec{s}_{k+1} + v \tag{1.23}$$

which is derived from a first order Taylor approximation of Equation (1.22). In this case the matrix $\tilde{H}$ is defined as:

$$\widetilde{H}_{ij} = \frac{\partial h_i}{\partial s_j} = \begin{cases} c_r(t_i - \tau_j)\exp(s_j)\Delta\tau, & t_i > \tau_j - \dfrac{\Delta\tau}{2} \\ 0 & t_i <= \tau_j - \dfrac{\Delta\tau}{2} \end{cases} \tag{1.24}$$

Equation (1.23) can be solved for s_{k+1} using the methods described in Section 1.3.1. When successive estimates of *s* are within a specified tolerance, the algorithm has converged. The 2-norm was used as convergence criteria. To find a decent starting point, the linear problem was solved first, and s then approximated as $(\kappa\text{-}1) - (\kappa\text{-}1)^2/2$.

Solutions using the exponential nonnegativity constraint for kernel Case 1 and injection Case 1 are shown in Figures 1.15 and 1.16.

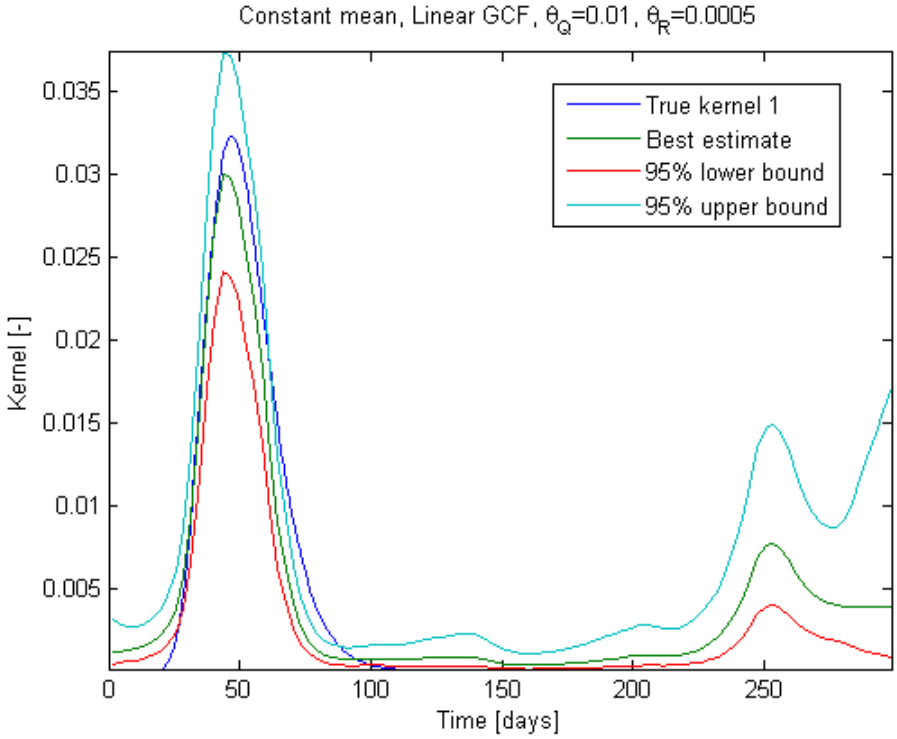

Figure 1.15: Best estimate and confidence intervals obtained for kernel 1, injection Case 1, using an exponential nonnegativity constraint.

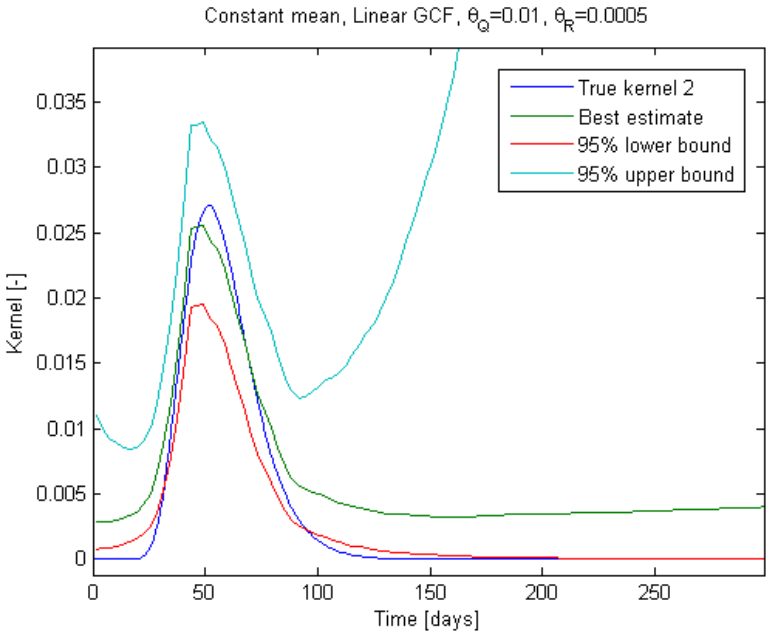

Figure 1.16: Best estimate and confidence intervals obtained for kernel 2, injection Case 1, using an exponential nonnegativity constraint.

As these figures show, the nonnegativity constraint does help quite a bit, especially with the smoothness of the solution ay late times. However, the upper confidence interval does tend to blow up at late times, where there is less constraining data. Another problem that was consistently encountered with this method was that the production data was poorly reproduced at late times. This is illustrated in Figure 1.17.

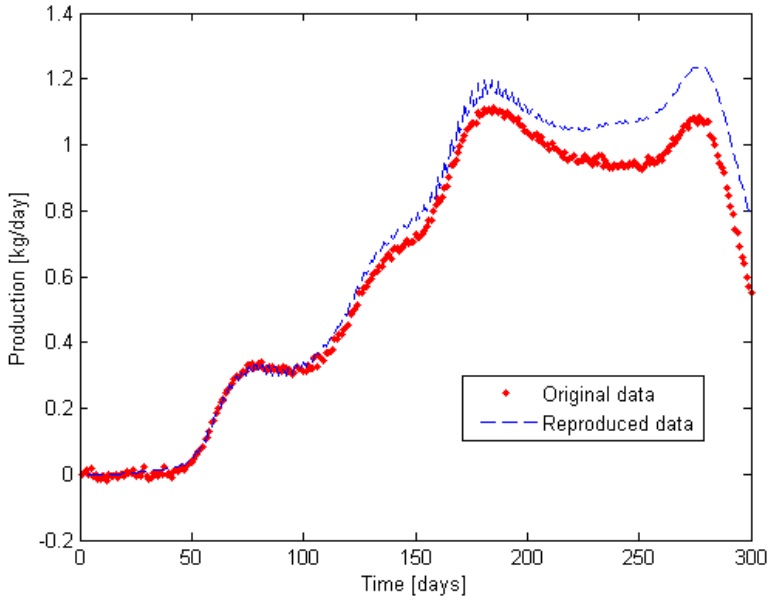

Figure 1.17: Data reproduction using an exponential nonnegativity constraint. The reproduction of data at late times was poor in most cases.

One way to get around the poor reproduction of data is to restrict the kernel estimation variable to a shorter time interval, i.e. a time that is closer to covering only the transient part of the kernel. For example by restricting the solution above (kernel Case 1 injection Case 1) to 150 days, the results shown in Figures 1.18 and 1.19 are obtained. The corresponding data reproduction is shown in Figure 1.20.

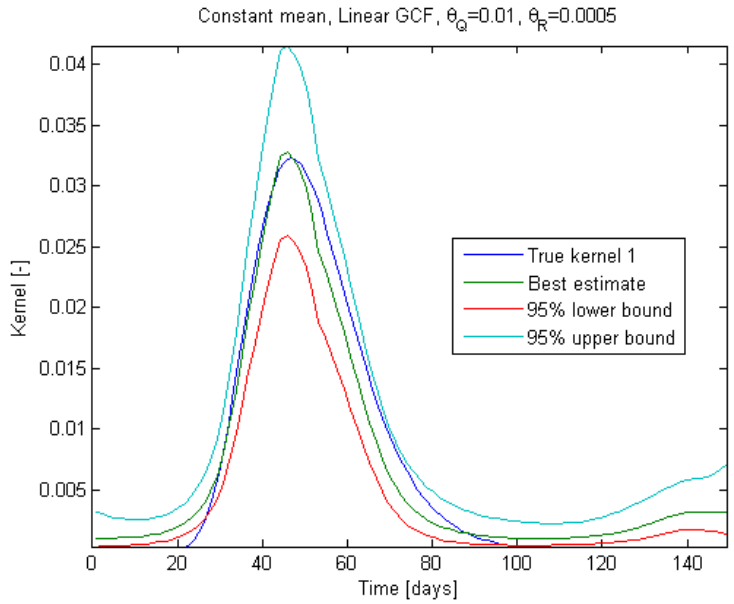

Figure 1.18: Best estimate and confidence intervals obtained for kernel 1, injection Case 2, using an exponential nonnegativity constraint, and a solution interval constrained to 150 days.

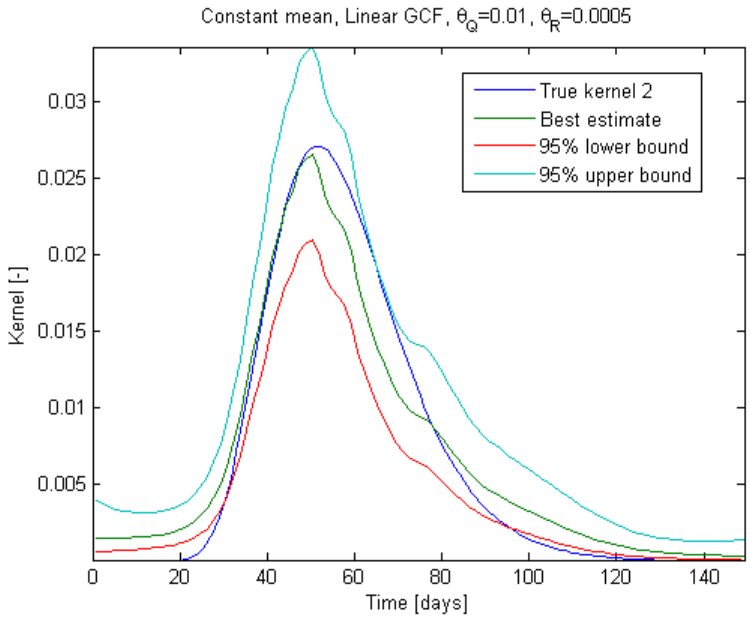

Figure 1.19: Best estimate and confidence intervals obtained for kernel 2, injection Case 2, using an exponential nonnegativity constraint, and a solution interval constrained to 150 days.

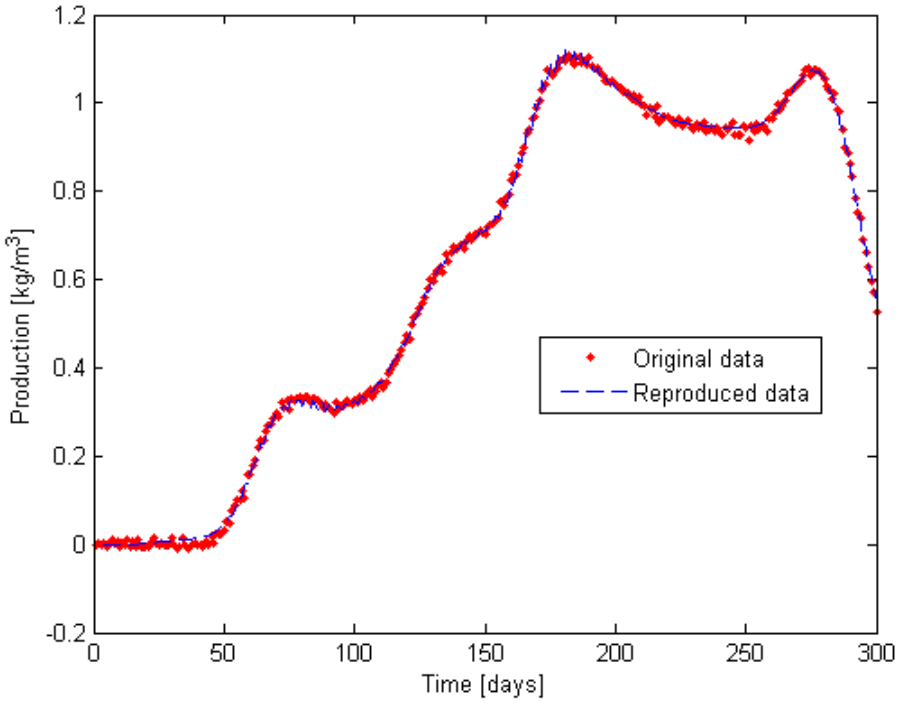

Figure 1.20: Data reproduction using an exponential nonnegativity constraint. The reproduction of data at late times improved significantly when the kernel solution was constrained to cover only the transient part.

Restricting the discretization of the kernel to a specific interval may be hard to implement in practice since the shape of the kernel is unknown *a priori*. However, the reproduction of the measurement data does improve as when the kernel solution is restricted to a certain interval, and it begins to degrade again when the solution interval is made too short (e.g. 50 days). Therefore, an automated search method for the optimal length of the discretization interval may be achievable.

1.4 FUTURE WORK

The examples in Section 1.3.2 have suggested a few topics of future research concerning the multiwell deconvolution method. A discussion of some of these follows.

Further experimentation with constraining the solution should be carried out. Different types of nonnegativity constraints could be implemented, e.g. setting $\kappa=s^2$. The problem can also be set up as a constrained minimization problem to be solved with powerful optimization packages. In that case, the constraint specified by Equation (1.21) could also be included. The problem to be solved would look something like the following:

$$\begin{aligned} \min_{\kappa,\beta} \quad & (\vec{c}_p - H\vec{\kappa})^T R^{-1} (\vec{c}_p - H\vec{\kappa}) + (\vec{\kappa} - X\beta)^T Q^{-1} (\vec{\kappa} - X\beta) \\ s.t. \quad & \kappa_j > 0, \quad j \in \{1,...,m\} \\ & \sum_{j=1}^{m} \kappa_{k,j} \Delta\tau \le 1, \quad k \in \{1,...,N_r\} \end{aligned} \tag{1.21}$$

A key question to be answered about problem (1.21) is whether the objective function is convex in the space of allowable solutions. If not, then the question is whether something can be done to make the objective function convex, thereby ensuring a unique and correct solution? For example, could the injection patterns be structured in such a manner that the solution will be more uniquely defined? Or could the roughness penalty term be modified to work better with the type of variability seen in the kernels?

As seen in the Section 1.3.2.3 (Example 3), some benefit may come from restricting the solution interval for the kernels to the time over which the kernel has the largest transient. Automated methods for finding an agreeable solution interval might be implemented, depending on the success of using other less restrictive methods.

Finally, it has been noticed that the solution to many of the examples investigated has been quite susceptible to noise in the data. Therefore it might be a good idea to use Monte Carlo methods to create multiple equivalent data sets with randomized noise (bootstrapping), and collect an array of solutions to obtain a smoother best estimate and more realistic confidence bounds.

1.5 CONCLUSIONS

Research during Spring quarter of 2009 has focused on multiwell deconvolution of tracer production data.

The deconvolution method can reveal, not only the travel time of tracer as discussed in the last quarterly report from Winter 2009, but it also has the possibility of revealing the dispersivity and fraction of tracer recovered for each injection-production well pair. Although a lot of data may have to be collected for this method to be applicable, it could save much time and provide important information pertaining to geothermal reservoir management, both at early and later stages of development.

The method introduced in this report is based on Bayesian statistics, which are used to create a linear system that balances the desire to reproduce data and obtain a smooth solution. Thus, the assumptions about the outcome are very minimal. The method does have a few nuances which are discussed through implementation of a few examples.

The future work discussed here pertains only to the multiwell deconvolution method. The main challenge is to pose the problem such that a unique and correct solution can be found. Hopefully the means for posing the problem in such a manner will yield to further research. Note that the entire scope of this research is more widely defined, as is discussed in the last quarterly report from Winter 2009.

2. FRACTURE CHARACTERIZATION OF ENHANCED GEOTHERMAL SYSTEMS USING NANOPARTICLES

This research project is being conducted by Research Associate Mohammed Alaskar, Senior Research Engineer Kewen Li and Professor Roland Horne. The objective of this study is to investigate the possibility of using nanotechnology to characterize the fracture system (direction, shape and size of fractures) in Enhanced Geothermal Systems (EGS).

2.1 SUMMARY

A trial nanoparticle injection into Berea sandstone was completed successfully. Silicon Oxide (SiO_2) nanoparticles were flowed through a Berea sandstone core. The injected nanoparticles were transported through the pore space of the rock and were detected in the effluent. Scanning Electron Microscopy (SEM) imaging demonstrated unambiguously that the nanoparticles had been transported through the pore network of the reservoir rock.

Prior to the nanoparticle injection experiment, the gas and liquid permeabilities, porosity and pore size distribution of the core sample were measured. It was found that the liquid permeability is about 61 md with a porosity of 18.5%. The pore size distribution measured by the mercury intrusion showed the core to have pore sizes as large as 10 micrometers.

This report describes nanoparticle characterization methods, details of permeability and pore size distribution measurements, and results of the initial nanofluid injection experiment.

2.2 INTRODUCTION

Last quarter (January-March 2009), the design and construction of the nanoparticle injection experimental apparatus was completed. The selection of nanofluid for initial testing was silicon oxide (SiO_2) with a narrow band of size distribution (50-130 nanometers) in ethanol solution. The injection and sampling strategies were also determined. In this quarter, the injection of the nanoparticles into a core was conducted. Standard measurements on the core sample were also performed. These measurements include the gas and liquid permeability, porosity and pore size distribution measurements.

2.3 NANOPARTICLES CHARACTERIZATION METHODS

Nanoparticles used in this study, and ultimately in the reservoir, need to be safe to handle and environmentally friendly (Kanj, Funk, and Al-Afaleg, 2007). Monodisperse silica particles (silicon oxide, SiO_2) satisfy all essential requirements and therefore have been selected for initial experimentation with nanofluid injection. The nanoparticle preparation has been accomplished by the hydrolysis of tetraethyl orthosilicate (TEOS) in aqueous ethanol solutions containing ammonia (Bogush, Tracy and Zukoski, 1988). SiO_2 can remain in suspension at different concentrations and particle sizes, and have a narrow band of sizes in solution.

In general, the quantity of the nanotracer produced at the sampling (exit point) should be sufficient to be recognizable and at concentrations above the lower detection limit of the

devices used to analyze the effluent and rock pore matrix by at least factor of three. Therefore, characterization of the rock as well as the nanofluid prior to and after injection was carried out by two different techniques, Dynamic Light Scattering (DLS) and Scanning Electron Microscopy (SEM).

2.3.1 Dynamic Light Scattering

DLS is a technique used to measure particles size suspended in liquid. It basically measures the random motion of suspended particles resulting from the bombardment of surrounding solvent molecules. This movement is known as Brownian motion. When particles are illuminated with a laser, the scattered light intensity varies depending on the size of the particles and hence their Brownian motion (www.malvern.com, n.d.). These changes in light intensity are related to particles size using the Stockes-Einstein relationship given by:

$$d(H) = \frac{kT}{3\pi\eta D} \tag{2.1}$$

where: $d(H)$ is hydrodynamic diameter, D is translational diffusion coefficient, k is Boltzmann's constant, T is absolute temperature and η is viscosity.

It should be mentioned that the particles size measured by DLS is the hydrodynamic diameter (how particles diffuse in a fluid). DLS assumes that the particle sizes being measured have same translational diffusion coefficient as spheres (Figure 2.1). Since the translational diffusion coefficient depends on various factors beside the particle core such as surface structure, concentration and the ion type of the medium, the reported size could be larger than the actual particles size (www.malvern.com, n.d.). Therefore, we used Scanning Electron Microscopy (SEM) imaging to confirm critical measurements.

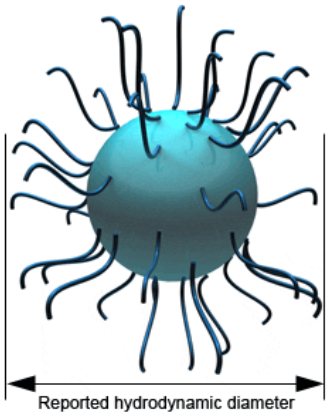

Figure 2.1: Measured hydrodynamic diameter by DLS (adopted from malvern.com technical library).

DLS was utilized to determine the particle size and distribution of the injected nanofluid and the effluent samples. These measurements were performed using the Zetasizer Nano

ZS manufactured by Malvern instruments. This device can detect particles as small as 0.6 nanometer.

2.3.2 Scanning Electron Microscopy

Microscopy-based techniques for particle size characterization provide a powerful tool for characterization of particle size, size distribution and morphology. A major advantage of microscopy-based technique is the capability to identify the particle shape (Jillavenkatesa, Ajit, Dapkunas, and Lum, 2001). This is particularly important in the nanofluid injection experiments because it enables us to distinguish the injected nanoparticles from preexisting objects such as fines and debris. Scanning Electron Microscopy (SEM) enables the evaluation of details at higher magnification and resolution and that makes it suitable for particles measurements in sizes below one nanometer.

The measurements were performed using a Philips FEI XL30 Sirion SEM instrument with Field Emission Gun source at the Stanford Nano-Characterization Laboratory. As mentioned earlier, SEM imaging is useful to confirm the DLS measurements which are simpler and cheaper but which do not distinguish between the particles other than by size. Moreover, SEM has been used to study the nanoparticle placement inside the rock matrix and how they arrange themselves in the pore spaces. In this regard, three different slices of the core at inlet, outlet and middle were cut and prepared for SEM analysis (Figure 2.2). Elaboration on the results is included in Section 2.5 of this report.

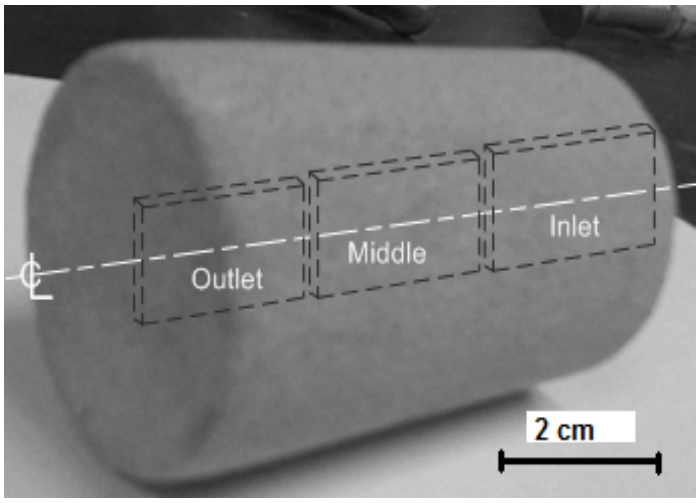

Figure 2.2: Rock sections for SEM analyses

2.4 EXPERIMENTS

This section provides the details of the first attempt to inject the nanofluid (SiO_2) into a core sample. Prior to nanofluid injection, pore size distribution and permeability measurements were conducted. Specification and calibration of all equipment and hardware can be found in the last quarterly report (January-March 2009). These include pressure differential and mass flow rate transducers, water and vacuum pumps and weight

balance. The first core sample tested was a Berea sandstone of 3.8 cm in diameter and 6 cm in length.

2.4.1 Pore Size Distribution

The pore size distribution of the core sample was measured by the mercury (Hg) intrusion method. The intrusion of mercury was performed using the AutoPore IV 9500 Mercury Porosimeter manufactured by Micromeritics. This porosimeter covers a pressure range up to 33,000 pound per square inch (psi) and pore diameter range from approximately 360 to 0.005 micrometer. The device has two low-pressure ports and one high-pressure chamber.

Prior to analysis, the sample must be weighed and all relevant sample information entered. Pressure points at which data are to be collected are then specified. Following that the sample is loaded into a penetrometer and is ready for measurements. The analysis is conducted in two stages, low-pressure and high-pressure. Firstly, the penetrometer is loaded in the low-pressure port to evacuate all gases and then backfilled with mercury. The data are collected at pressures up to 30 psi. Secondly, the penetrometer is removed and installed in the high-pressure chamber. The analysis is resumed and data are collected up to pressure as high as 33,000 psi. The principal idea behind the pore volume measurements is as follows. The pore volume data are generated through the calculation of the volume of mercury left in the penetrometer stem as pressure is applied. As pressure increases, mercury from the penetrometer stem is forced to enter the pores. Smaller pores require higher pressure to overcome capillarity. Mercury is the nonwetting phase, and its surface tension, contact angle and radius of curvature are used to obtain the pore diameter at a given pressure (Micromeritics, 2008).

Measurements conducted on the Berea sandstone showed the core to have pore sizes as large as 10 micrometers (Figure 2.3). Thus, theoretically, most of the nanoparticles (50-130 nanometer size range) should be able to pass through the core.

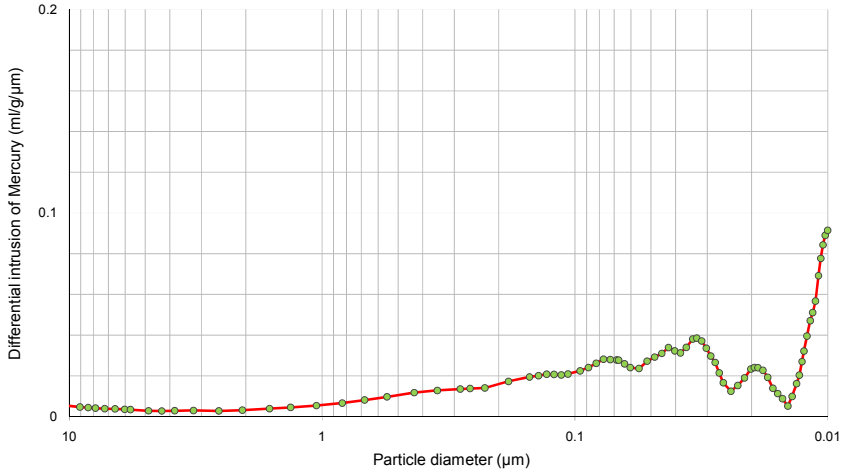

Figure 2.3: Pore size distribution of Berea sandstone core

2.4.2 Permeability Measurement

First, the gas permeability was measured. The Klinkenberg effect (gas slippage) was considered to evaluate the equivalent liquid permeability. Second, the liquid permeability for the same core sample was also measured.

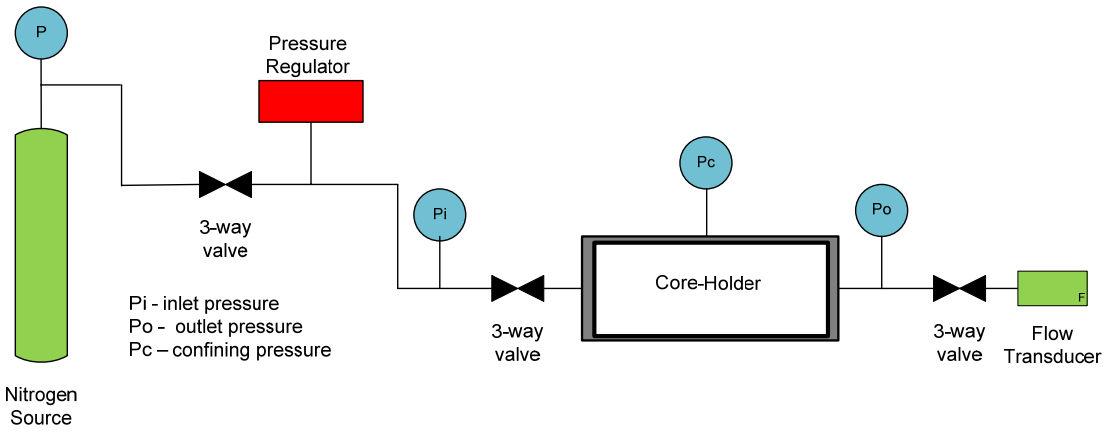

Figure 2.4: Schematic of the apparatus for measuring gas permeability.

Figure 2.4 is a schematic of the apparatus used in the measurement of gas permeability. The gas flowed in this experiment was Nitrogen (N_2). The inlet and outlet pressures were measured using differential pressure transducers of different ratings. The flow rate at the outlet was measured using a mass flow rate meter. Calibration curves were included in the last report (January-March 2009).

The core was first dried in a furnace at 100°C under vacuum for 24 hours. After weighing the core sample, it was placed inside the core-holder under a confining pressure of 500 psig. The gas permeability measurement was then started by introducing Nitrogen at different flow rates and inlet pressures. The average gas permeability was found to be around 174 md by applying Darcy's law for compressible fluids which is given by:

$$k_{gas} = \frac{2\mu p_{out} q_{out} L}{A(p_{in}^2 - p_{out}^2)} \tag{2.2}$$

where μ is the viscosity in centipoises, q_{out} is outlet volumetric flow rate in cubic centimeter per second, A is the core cross-sectional area in square centimeter, L is the core length in centimeter and p_{in} and p_{out} are inlet and outlet absolute pressures in atmospheric unit, respectively.

The gas permeability as a function of the reciprocal of mean pressure is depicted in Figure 2.5. According to the Klinkenberg effect, extrapolating the straight line to infinite mean pressure (or zero reciprocal of mean pressure) intercepts the permeability axis at a point

designated as the equivalent liquid permeability (Amyx, Bass, and Whiting, 1960). In Figure 2.5, the average equivalent liquid permeability is 86 md.

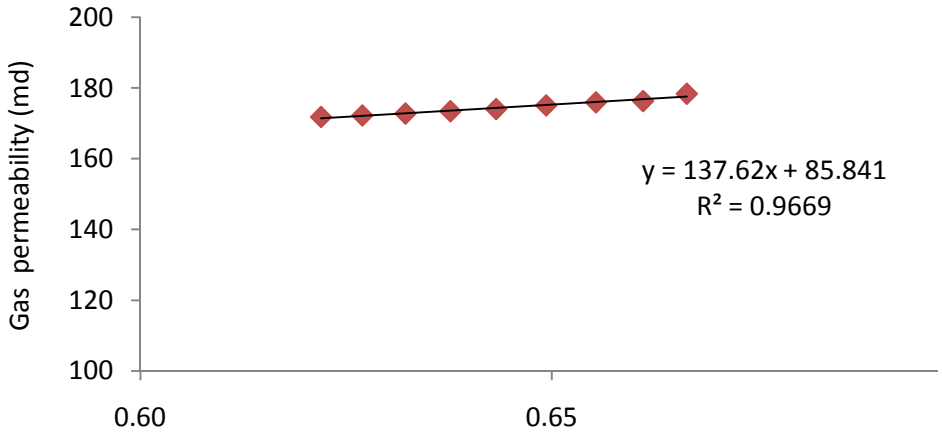

Figure 2.5: Gas permeability versus the reciprocal of mean pressure

The liquid permeability was measured on the same core sample. A schematic of the apparatus used in the measurement of liquid permeability is shown in Figure 2.6.

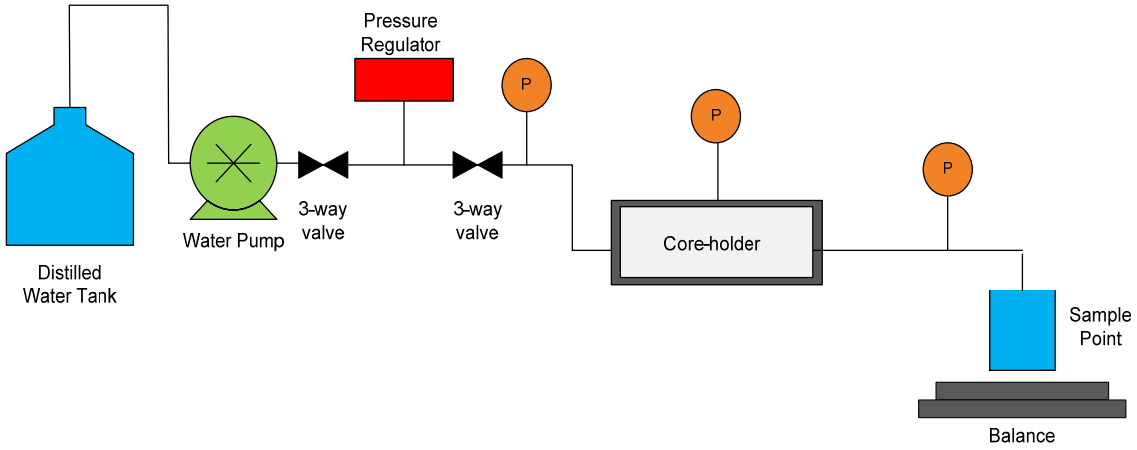

Figure 2.6: Schematic of apparatus for liquid permeability measurement

The core sample was first saturated with water outside the core-holder. The core and related system were evacuated using a Welch Vacuum Pump for 4 hours at a vacuum pressure of about 30 millitorr to remove moisture. Distilled water was introduced to completely submerge the sample. The core was then left submerged overnight and the remaining vacuum released to aid the process of saturation. After that the core was removed and wiped dry to remove excessive water on surface. Finally, the core was weighed and hence the its porosity calculated. The core turned out to have a porosity of around 18.4 % and a pore volume of 12.5 cubic centimeters. The porosity calculation is as follows:

$$\phi = \frac{V_p}{V_B} * 100 \tag{2.3}$$

$$V_p = W_s - W_d \tag{2.4}$$

$$V_B = \pi r^2 l \tag{2.5}$$

where ϕ is the porosity in percentage, V_p and V_B are pore and bulk volumes in cubic centimeter, respectively. W_s and W_d are the weight of core after and before saturation, in gram, respectively. r and l are the radius and length of the core in centimeter, respectively.

The same differential pressure transducers were used as previously in the gas permeability measurement. In addition, a water pump was used to inject distilled water. The minimum pumping rate of the pump is 0.05 ml/min with an accuracy of 0.01 ml/min. The pump calibration curve can be found in the last report (January – March 2009).

Following the saturation, the liquid permeability was measured by injecting distilled water using the water pump. Several flow rates were used to calculate the liquid permeability, ranging from 10 to 30 ml/min at different differential pressures. Darcy's law for horizontal flow was utilized to compute the permeability. Darcy's law for horizontal flow is given by:

$$k_{liq} = \frac{q\mu L}{A\Delta p} \tag{2.6}$$

where q is the volumetric flow rate in milliliter per second, μ is the viscosity in centipoise, L and A are the length and the cross-sectional area of the core in centimeter and square centimeter, respectively. Δp is the differential pressure across the core sample in atmospheres.

The average liquid permeability was found to be around 61 md. Various estimated permeability values are plotted against the flow rate in Figure 2.7. A slight change of about 1 md was observed in the permeability measurements as the flow rate changes.

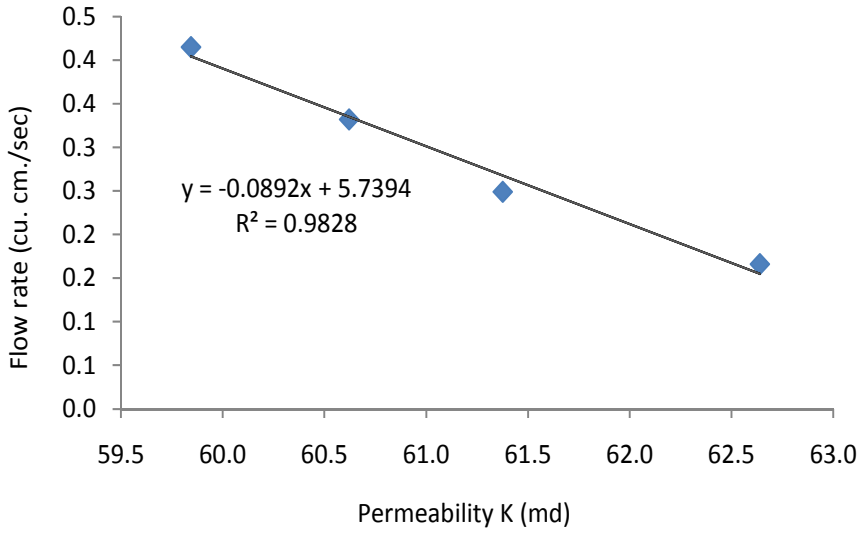

Figure 2.7: Liquid permeability measured at different flow rates.

2.4.3 Nanofluid injection experiment

To explore the possibility of using the nanoparticles to characterize the fractures, an experimental investigation was initiated to assess a suitable particle size and to verify their transport through the formation rock. The same coreflooding apparatus was used. A schematic of the apparatus is shown in Figure 2.8. Nanofluid solution was contained in a pressure vessel downstream of the water pump. The nanofluid was injected into the core with the aid of nitrogen pressure. The configuration also allows for injection of particle-free water, without interrupting the flow.

This experiment did not consider the temperature effect, so was conducted at room temperature. The nanofluid prepared contained silicon oxide (SiO_2) particles of sizes between 50 and 130 nanometers. It is of interest to inject the nanoparticles with a variation of size and determine which sizes come out in the effluent.

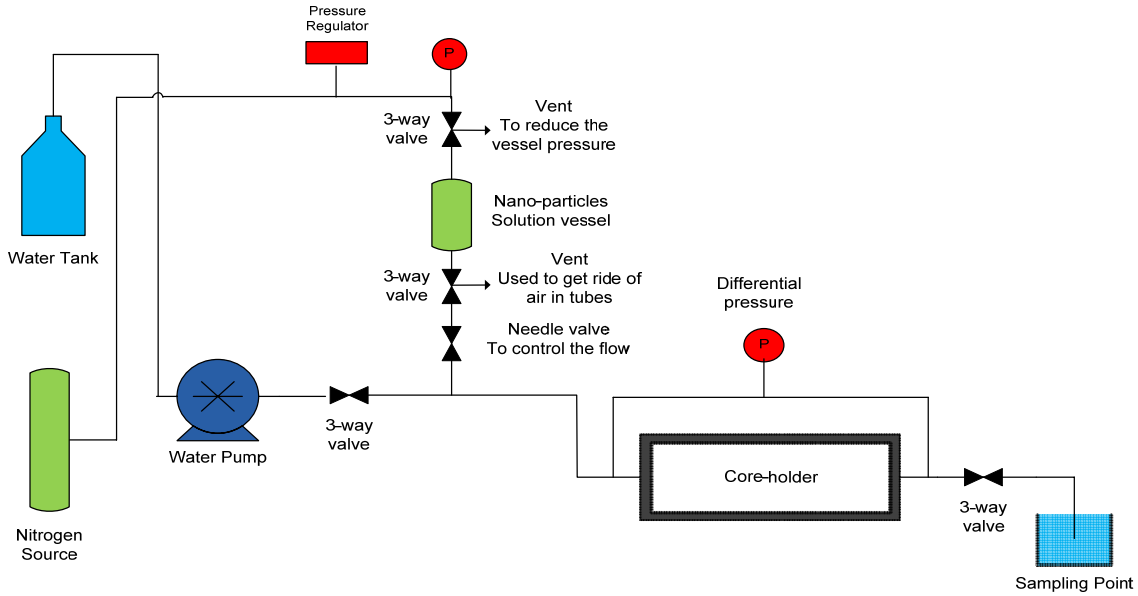

Figure 2.8: Experimental apparatus for nanofluid injection.

The nanofluid injection sequence is similar to the process suggested by Kanj et al. (2007). The sequence involves the injection of a pore volume of nanofluid followed by a continuous injection of pure water. The pore volume was determined as outlined in Section 2.4.2. In particular, two pore volumes plus the dead volume (the volume of the tubes and fittings) were injected. The dead volume is required to fill the tubes completely prior to nanofluid entering the core. Following that is the first pore volume which should fill the pore spaces. The second pore volume is used to confirm the filling. The volume calculations are straightforward:

$$V_p = V_B \phi \tag{2.7}$$

$$V_d = \pi r_t^2 l_t \tag{2.8}$$

$$V_{inj} = V_p + V_d \tag{2.9}$$

where r_t and l_t are the radius and length of the tube in centimeter, respectively. V_d and V_{inj} are the dead and total injected volumes in cubic centimeter, respectively. The rest of parameters have their usual definition.

Subsequent to the injection of the nanofluid (pore and dead volumes), a continuous flow of pure water was introduced. Specifically, six pore volumes of pure water were injected while the effluent samples were collected. The total time of the experiment was approximately two and half hours. The injection was at the rate of one milliliter per minute to facilitate the sampling operation. A total of 45 effluent samples were collected. Not all these samples were analyzed but rather a careful selection of some was done to optimize the analysis time. The infrequently selected samples have indicated the trend of the

returning nanotracer and more details (if needed) can be obtained by analyzing the samples in between.

2.5 RESULTS

Silicon Oxide (SiO_2) nanoparticles were flowed successfully through a Berea sandstone core. The injected nanoparticles were transported through the pore space of the rock and were detected in the effluent. We were able to verify recovery of the nanoparticles following their injection, and to demonstrate that they were not trapped in the pore spaces by hydraulic, chemical or electrostatic effects. The SiO_2 nanoparticles had a relatively narrow distribution of size between 50 – 130 nanometers (Figure 2.9). The nanoparticles were easily distinguishable from the core fines and debris due to their size and spherical shape, even though all are made of same material as the rock itself (silica).

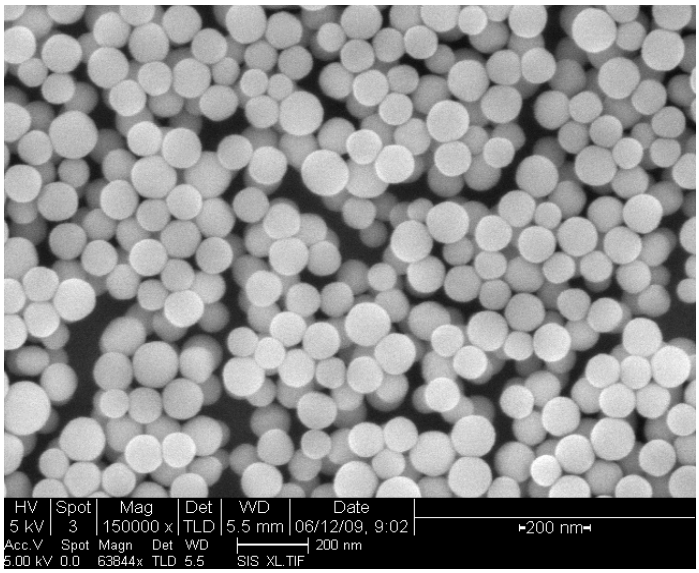

Figure 2.9: SiO_2 nanospheres in the injected nanofluid. Image obtained by SEM.

The effluent samples were examined for the existence of the nanoparticles using the DLS technique. For instance, an effluent sample at the fifth Pore Volume Injected (PVI) shows a particle size distribution as depicted in Figure 2.10.

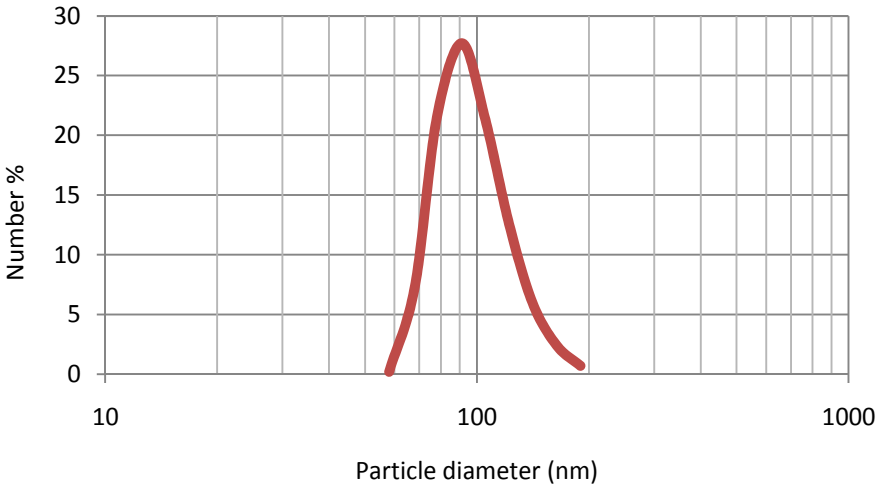

Figure 2.10: Particle size distribution by number percentage of an effluent sample at the fifth PVI (Courtesy of Malvern Instruments)

The more precise approach using SEM imaging of the effluent confirms this finding (Figure 2.11). The average nanoparticle size in Figure 2.11 is around 100 nanometers.

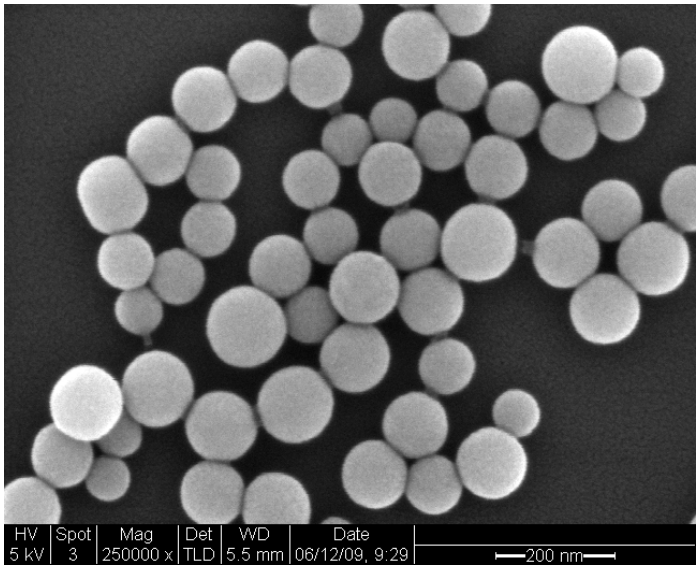

Figure 2.11: SEM image showing SiO_2 nanoparticles in the effluent.

It is worth mentioning that larger size particles than injected (SiO_2 nanofluid) were detected by DLS in some of the early effluent samples. An example of the size distribution based on the number percentage of particles is illustrated in Figure 2.12. It is believed that these particles are the core fines which are produced from within the rock pore spaces.

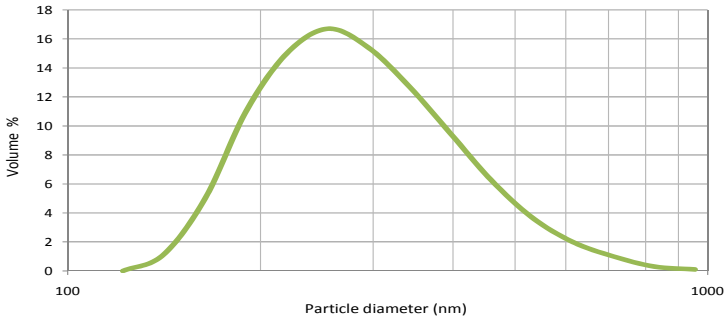

Figure 2.12: Particle size distribution by number percentage of effluent sample containing core fines and debris (Courtesy of Malvern Instruments).

To verify this hypothesis, SEM images of the same sample were taken, for example as shown in Figure 2.13. The presence of such fines has resulted in the size distribution estimated by light scattering technique shown in Figure 2.12.

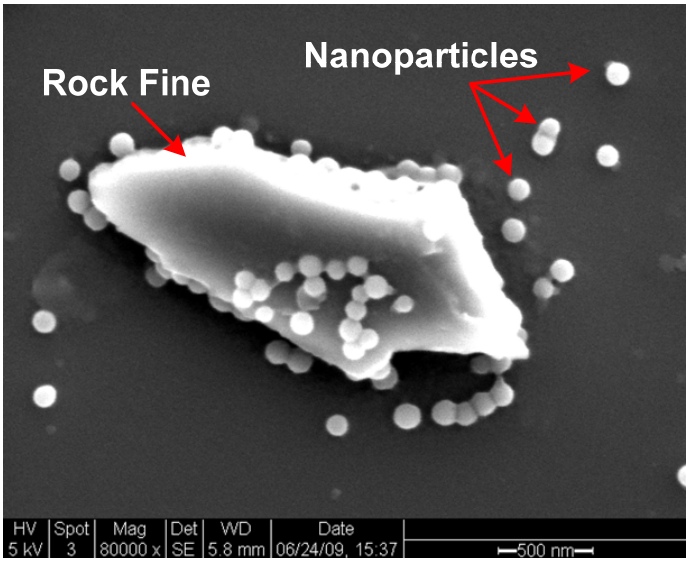

Figure 2.13: SEM image of rock fine relative to injected nanoparticles.

These larger particles showed up right after the injection of the two pore volumes of nanofluid plus the dead volume of the tubes. Traces of these particles had been detected within the first injected pore volume of distilled water with a decreasing trend as depicted in Figure 2.14. The larger particles were only produced in the early part of the injection. In Figure 2.14, each particle size is plotted individually, showing its volume percentage as function of PVI. Recall that the pore volume of this core is approximately 12 milliliters. The injected volume axis shows only a couple of milliliters from the first PVI until the end of the sixth pore volume of water. So it can be concluded that these larger size fines and

debris have been produced or that the core's pore spaces have been washed out during the injection process.

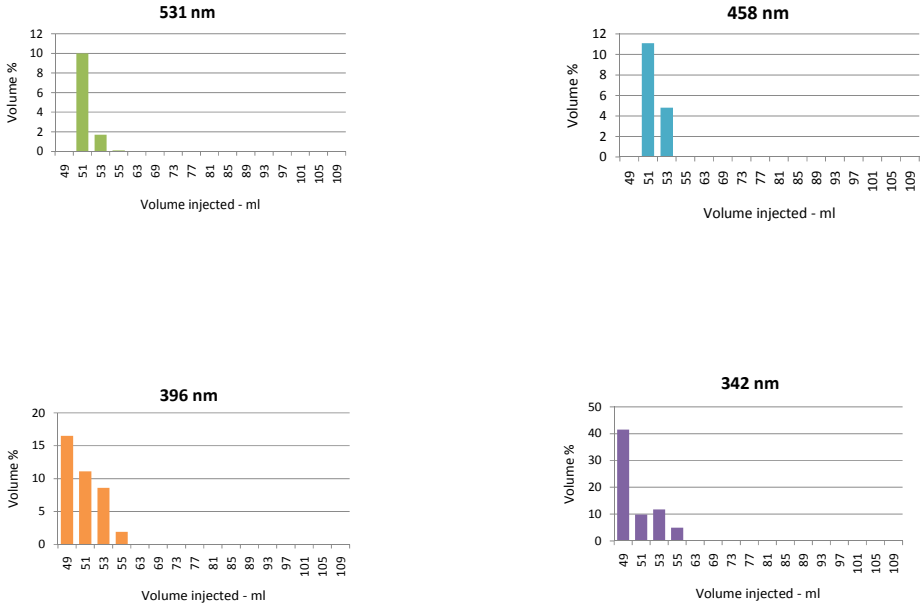

Figure 2.14: large particles (core fines and debris) as function of pore volumes injected PVI.

Based on the pore size distribution measured by mercury intrusion (0.01 to 10 micrometers pore diameters), the nanoparticles should be able to pass through the core. This hypothesis was further confirmed in Figure 2.15 by generating similar plots as Figure 2.14 for particle sizes within the range of the injected SiO_2 nanoparticles (50 to 130 nanometers). Smaller particles have not been detected by DLS at earlier PVIs because larger particles act as a shadow over smaller ones and therefore they are not detected by DLS. Smaller nanoparticles were produced constantly in all pore volumes throughout the injection. It has been observed, however, the continuous injection of six pore volumes was not enough to show a pattern of tracer concentration as function of injected volumes and hence time. Nanoparticles continued to be produced from the core until the end of the injection, indicating that some of them had resided in the core beyond the end of particle injection but were slowly being flushed out. This was confirmed later by sectioning the core and looking inside it using SEM imaging.

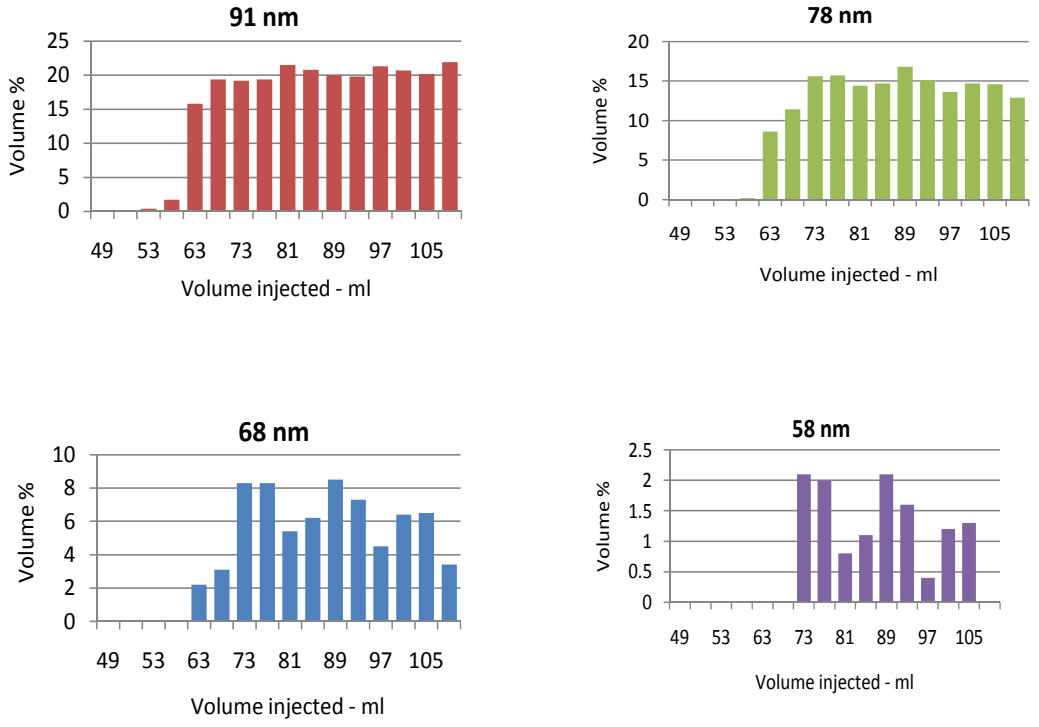

Figure 2.15: Particles volume percentage as function of pore volume injected PVI.

The production history of injected nanoparticles is better illustrated by plotting their volume percentage as it varies with time (Figure 2.16). It is expected that the concentration of each nanoparticle should decrease as more pore volumes of distilled water are injected. It is evident from the production history plots that we should have injected more pure water following the partcles to be able to detect the maximum particle concentration peak.

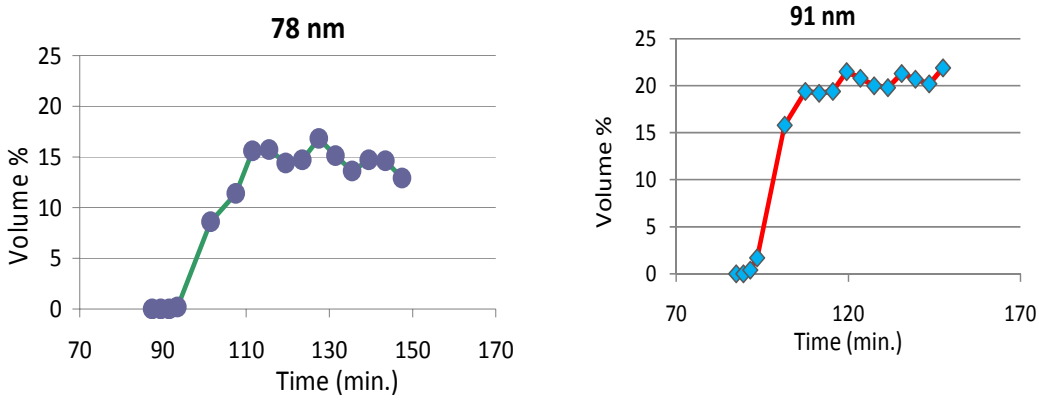

Figure 2.16: Production history of nanoparticles of sizes 78 and 91 nanometers.

Subsequent to the analysis of the effluent, the interior of the rock itself was examined. Specifically, middle and outlet slices were examined most closely because nanoparticles

present in those sections had clearly passed the inlet. Figure 2.17 shows an SEM image of the pore spaces at the middle section of the core. The SiO_2 nanoparticles are visible as little white spheres. These spheres are approximately 100 nanometers in diameter. This demonstrates unambiguously that the nanoparticles had been transported through the pore network of the reservoir rock.

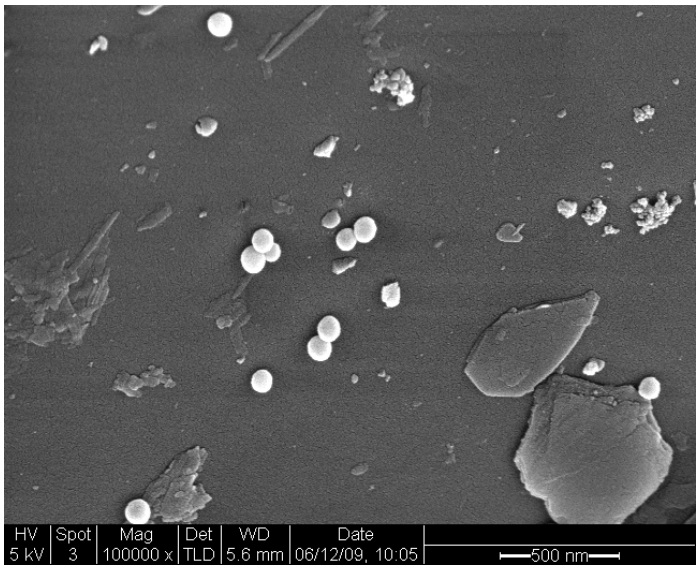

Figure 2.17: Nanoparticles at the middle section of the rock. Non-spherical objects are natural fines and debris from the rock itself.

In terms of characterizing the fractures in the rock, which is the primary objective of the project, these preliminary experiments show promise. Figure 2.18 shows that the nanoparticles passed through pores of sizes larger than themselves, but were unable to pass into the tinier natural fractures that exist within the rock structure. A slightly smaller nanoparticle could have entered the fracture.

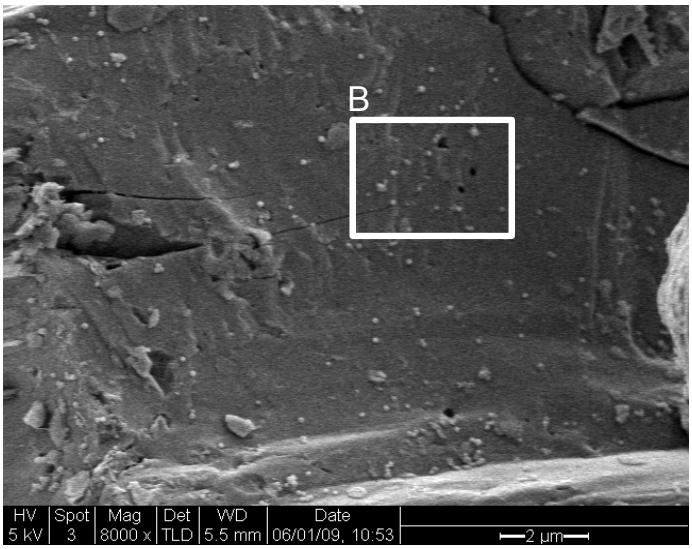

(A)

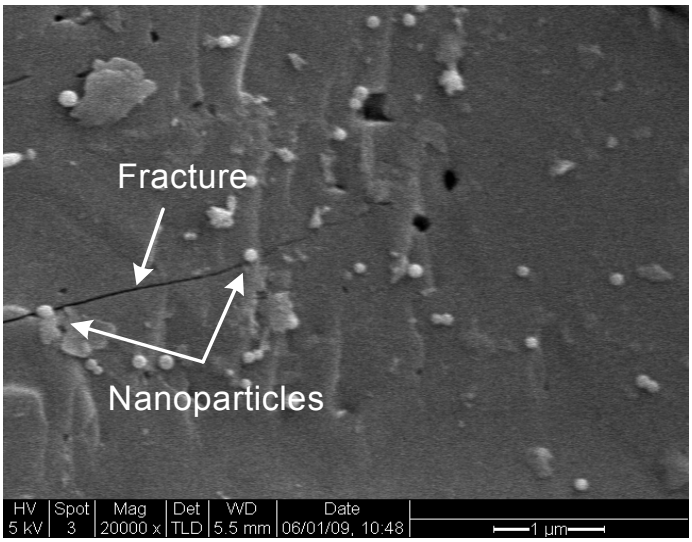

(B)

Figure 2.18: Natural fracture with two nanoparticles at its entry.

2.6 FUTURE WORK

The next stage of the project will be to inject the nanoparticles into fractured rock that has much tighter pore spaces in the rock matrix. Therefore, greywacke rock from The Geysers geothermal field has been selected for the next nanofluid injection experiments. Preliminary experimentations (liquid permeability) with the greywacke core show that the rock has very low matrix permeability. Furthermore, the pore size distribution is in the range of 6 to 150 nanometers as shown in Figure 2.19. We plan to inject a nanofluid with relatively wide size distribution (i.e. nanoparticles in size of 30 to 350 nanometers). The

production history of returned nanotracers is expected to show selective recovery, in which only smaller nanoparticles are transported through the rock.

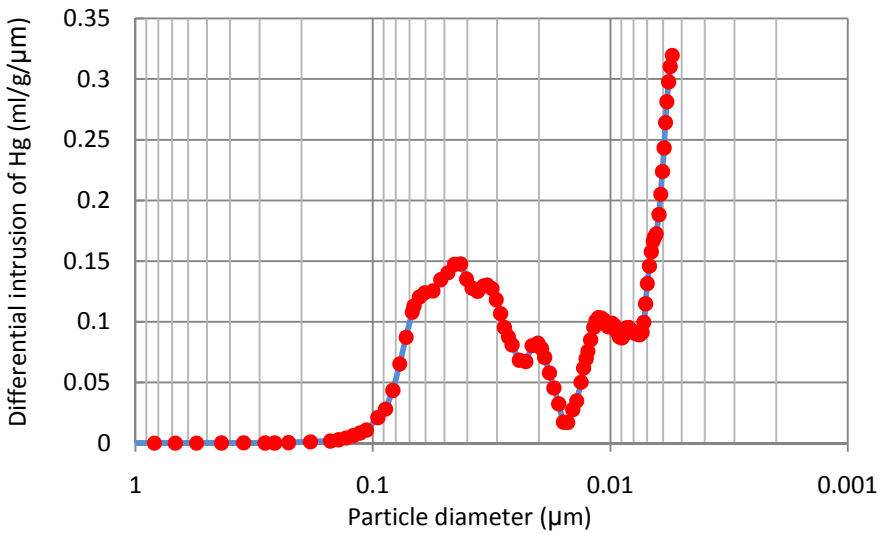

Figure 2.19: Pore size distribution of greywacke rock from The Geysers.

3. REFERENCES

Amyx, J. W., Bass, D. M. Jr., and Whiting, R. L. (1960), *Petroleum Reservoir Engineering, Physical Properties.* McGraw-Hill Book Co.

Axelsson, G., Flovenz, O.G., Hauksdottir, S., Hjartarson, A. and Liu, J.: *"Analysis of tracer test data, and injection-induced cooling, in the Laugaland geothermal field, N-Iceland,"* Geothermics, Volume 30(6), December 2001.

Bogush, G. H., Tracy, M. A., and Zukoski, C. F., IV., "Preparation of Monodisperse Silica Particles: Control of Size and Mass Fraction," *Non-Cryst. Solids* **104** (1988) 95.

Dynamic Light Scattering: Introduction in 30 Minutes. No Date. Malvern Instruments Technical Library. Retrieved on April 03, 2009 from http://www.malvern.com/common/downloads/campaign/MRK656-01.pdf

Fienen, M.N., Luo, J. And Kitanidis, P.K.: *"A Bayesian geostatistical transfer function approach to tracer test analysis,"* Water Resources Research, Volume 42(7), 2006

Jillavenkatesa, Ajit, Dapkunas, S. J. and Lum, L. H., " Particle Size Characterization," Materials Science and Engineering Laboratory, National Institute of Standards and Technology, Washington, Special Publication 960-1, 2001

Juliusson E. and Horne, R.N.: *"Fracture characterization using production and injection data,"* Setcion 1, DOE quarterly report (2009 January to March), Contract DE-FG36-08GO18192, Stanford Geothermal Program, Stanford University, California, April 2009.

Kanj, M., Funk, J. and Al-Afaleg, N., "Towards In-situ Reservoir Nano-Agents," Saudi Aramco, Dhahran, Saudi Arabia, 2007.

Kitanidis, P.K., *"Applied Stochastic Inverse Problems,"* unpublished textbook for class CEE362G, Stanford University, winter quarter 2009.

Lovekin, J.: *"Optimization of injection scheduling in geothermal fields,"* MS thesis, Stanford University, Stanford, CA, 1989.

Micromeritics Autopore IV 9500, Operator's Manual V. 1.09, Part No. 950-42801-01, April 2008.